The Polarimetric Impulse Response and Convolutional Model for the Remote Sensing of Layered Vegetation

Tyler C. Kramer

Thesis submitted to the Faculty of the
Virginia Polytechnic Institute and State University
in partial fulfillment of the requirements for the degree of

Master of Science
in
Electrical Engineering

Dr. Gary S. Brown	Committee Chair
Dr. Steven W. Ellingson	Member
Dr. Wayne A. Scales	Member
Dr. Bradley A. Davis	Member

5 March 2007
Blacksburg, Virginia

Keywords: Remote Sensing, Scattering, Random Volume, Impulse Response

The Polarimetric Impulse Response and Convolutional Model for the Remote Sensing of Layered Vegetation

Tyler C. Kramer

(ABSTRACT)

To date, there exists no complete, computationally efficient, physics-based model to compute the radar backscatter from forest canopies. Several models attempt to predict the backscatter coefficient for random forest canopies by using the Vector Radiative Transfer (VRT) Theory with success, however, these models often rely on purely time-harmonic formulations and approximations to integrals. Forms of VRT models have recently been developed which account for a Gaussian pulse incident waveform, however, these models often rely heavily on very specific and obfuscated approximations to solve the associated integrals.

This thesis attempts to resolve this problem by outlining a method by which existing, proven, time harmonic solutions to the VRT equation can be modified to account for arbitrary pulse waveforms through simple path delay method. These techniques lend physical insight into the actual scattering mechanisms behind the returned waveform, as well as offer explanations for why approximations of previous authors' break down in certain regions. Furthermore, these radiative transfer solutions can be reformulated into a convolutional model which is capable of quickly and accurately predicting the radar return of random volumes. A brief overview of radiative transfer theory as it applies to remote sensing is also given.

This work received support from the United States Air Force under SBIR contract FA8651-05-C-0231.

Acknowledgements

The Author would first like to thank his advisor, Dr. Gary Brown, for his support and guidance throughout the course of this project. It has been an an honor to work under him in the Electromagnetic Interactions Lab over the past two years. I would also like to thank Dr. Steven Ellingson and Dr. Wayne Scales for their comments and insights into this topic. I am also very grateful to Dr. Bradley Davis whose previous work provided much of the basis for this project.

I would also like to thank Dr. Richard O. Claus and his company, NanoSonic, Inc., for supporting me early on in the course of this project.

Finally I would like to thank my parents Curt and Dee, for their endless love and support. Only through their constant encouragement have I been able to reach this milestone.

Contents

List of Figures

List of Tables

Chapter 1

Introduction and Review of Literature

Remote Sensing has a wide range of applications, such as the sensing of soil and vegetative parameters for civilian and agricultural use and the detection and identification of targets for military use. However, there still exists very few accurate models to predict how a electromagnetic wave will propagate through a region of scatterers realized by the vegetation. A full wave solution, while accurate, is impossible to model due to the complex nature of most natural vegetation. The most common models, therefore, are based on Radiative Transfer (RT) theory, which relies on the propagation of incoherent power through the Vector Radiative Transfer Equation (VRTE).

Issues with the VRTE approach arise when more detailed information needs to be extracted from data collected from real-world systems. When the applications are target detection or biological/geophysical monitoring, parameter extraction becomes very difficult. This paper will address this problem by using field-proven RT theory to develop an alternative model for the remote sensing of random volumes.

In Chapter 2, the Radiative Transfer theory technique and equations will be introduced for both the scalar and vector cases. The equations' relationship to electromagnetic propagation and scattering will be discussed through the introduction of the Stokes vectors (parameters). The iterative solution to the VRTE will be discussed along with the limitations associated with such solutions as well as with the Radiative Transfer theory itself. This chapter will provide much of the theoretical frame work for the remaining chapters and thesis topic.

In Chapter 3, VRTE-based remote sensing models will be introduced. This section will focus on the Michigan Microwave Canopy Scattering Model (MIMICS) which was successfully used to model backscatter from orchards in the microwave regime. The model's layered geometry will be discussed, and the first order solution to the corresponding VRTE will be given. Within each layer, the dominating scattering mechanism(s) will be reviewed and examples

Figure 1.1: Synthetic Aperture Radar image of Washington, D.C. (Courtesy of Sandia National Laboratory [Sandia National Laboratories, 2005]).

of scatterers provided and verified. More recent advances and additions to the MIMICS, such as bistatic scattering and multi-layer foliage models, will also be discussed relative to the scope of this thesis.

In Chapter 4, the recent works into the Pulsed Vector Radiative Transfer Equation (PVRTE) will be discussed and their applications layered vegetation explored. A physical interpretation of the VRTE and a subsequent path delay method technique will be developed, capable of the modifying the time-harmonic VRTE of previous sections for the case of an arbitrary pulse. The resulting solution will then be compared to others obtained from more rigorous analysis techniques. Finally, a simple impulse response for first order random volume scattering will be derived.

Finally, Chapter 5, the impulse response of the previous chapter will be tied together into a complete convolutional model in order to predict the backscatter from a multi-layered forest canopy or random volume from a radar system with a finite beamwidth. Various models and approximations will be derived and simulated.

1.1 Radiative Transfer

The authoritative source on Radiative Transfer Theory as applied to electromagnetic propagation is [Ishimaru, 1997]. Much of the current and past work involving this technique has revolved around this work. Further theory can be found in [Tsang et al., 1985] which presents the work in a more applied form.

Most of the applied radiative transfer work in remote sensing was done by two groups over the past two decades. Dr. Fawwaz Ulaby, working out of the University of Michigan, developed a complete model which he dubbed the Michigan Microwave Canopy Scattering model, or MIMICS. This model divided the vegetation into three regions: a crown layer consisting of small cylinders and discs, a trunk layer consisting of near-vertical cylinders, and a specular ground interface. Any surface roughness was generally assumed to be small, and scattering from rough surfaces was accounted for through a non-physical correction factor. MIMICS only took into account first order scattering. This model was validated by applying it to walnut orchards and other well maintained orchards and fields.

Similar work was done at the University of Texas during the same period by a group led by Drs. Mohammed Karam and Adrian Fung [Karam et al., 1992]. Their model was very similar to the MIMICS model of Ulaby, except it accounted for higher-order scattering between each layer and included the scattering from rough surfaces without the use of a non-physical "correction factor".

Both of these applications dealt only with the return of a time-harmonic wave from a vegetative layer. Therefore, only the backscatter from a single frequency could be modeled. This was an inherent disadvantage as pulsed-radar was and remains much more common and useful in most situations. Recent works by [Chang and Jin, 2002] have attempted to solve this problem using a complicated form of the Pulse Vector Radiative Transfer Equation (PRVTE), however, the developed models rely on approximations and offer little physical insight into the scattering process. Furthermore, only the foliage scattering is considered and any effect of the radar system is neglected.

1.2 Convolutional Model

The Convolutional Model as it appears in this paper attempts to expand and improve upon a model developed by Dr. Bradley Davis working through the Electromagnetic Interactions Laboratory at Virginia Tech [Davis, 2000]. This work was based on the work by Dr. Gary Brown and his paper [Brown, 1977] which introduces the impulse response method to pulse scattering from rough surfaces. Further work on this topic was done by Dr. Robert Adams in [Adams and Brown, 1998] which applies this method to scattering from a rough surface over a penetrable medium. Similar work in the time domain was also done by Schwering et al. in [Whitman et al., 1996]. This work focused on the issue of land-to-land propagation through the forest.

The advantage to these approaches is that they are all in the time domain and based on the Radar Equation. As a result, parameters such as antenna beamwidth and signal to noise ratios can also be analyzed relative to the scattering process. Furthermore, as the name

implies, these models are capable of using a convolutional approach: i.e., complex integrations can be brought into an alternate domain through the use of Fast-Fourier Transforms (FFT) and multiplied rather than integrated. However, the existing models are all scalar and cannot easily account for the effects of polarization. Furthermore, most remain untested on forests or vegetation.

1.3 Goal of Thesis

The goal of this thesis is therefore twofold. First, a novel path delay technique will be developed which will allow preexisting time-harmonic solutions to the VRTE, such as those in [Ulaby et al., 1990], to be modified to model the response of an incident arbitrary pulse waveform. This method will yield an equation identical to those obtained by [Chang and Jin, 2002] through a more rigorous analysis. However, not only is the ray-tracing technique simpler to implement, it also provides more physical insight into the behavior of the underlying equations and propagation through the media.

The second goal of this paper is to use the derived time-domain solution to the VRTE to obtain the impulse response of a layer(s) of foliage. This impulse response can be explicitly computed using a convolution. By deriving and defining an impulse response, a quick, efficient and thorough analysis can be performed on the scattering from a random volume illuminated by a radar.

1.4 Comment on Notations

In writing this thesis, the Author made every attempt to be clear and consistent in the notation while still adhering to the most common variable names used in modern Radiative Transfer theory. However, as any brief survey of literature will show, due to the parallel development of RT theory at various laboratories as well as the heuristic nature of the theory itself, there exists no "unified" terminology. Therefore, every attempt was made to use the most commonly referred to labels and definitions whenever possible. Furthermore, in order to simplify the appearance of the equations in this paper, the spatial dependences of most quantities were not explicitly written. In order to compensate for these factors, Appendix A contains a list of common terms used throughout this thesis as well as their (1) common name, (2) secondary names, (3) definition, and (4) notations.

Chapter 2

Radiative Transfer Theory

Radiative Transfer Theory was first introduced into the realm of physics through Chandrsekhar in order to estimate the black body radiation effects experienced in astrophysics [Chandrasekhar, 1960]. Significant work was later done by Akira Ishimaru in order to relate the Radiative Transfer equations into the field of electromagnetics. Much of this work can be found in [Ishimaru, 1997].

Instead of propagating the electric and magnetic fields through a region of scattering elements, radiative transfer theory propagates incoherent "intensities" or power. While this approach is heuristic in nature, it does maintain a certain degree of physics behind it by relying on electromagnetic theory to determine expressions for the scattering of individual elements. This theory also assumes that the region of scatterers is sparsely populated, thereby allowing for the assumption that there is no coupling between elements and the power can be incoherently added instead of adding the corresponding electric fields.

2.1 The Scalar Radiative Transfer Theory & Equation

The basic equation to describe Radiative Transfer Theory is given by

$$\frac{\partial}{\partial s} I(\vec{r}, \hat{s}) = -\rho \sigma_t I(\vec{r}, \hat{s}) + \iint_{4\pi} P(\hat{s}, \hat{s}') I(\vec{r}, \hat{s}') d\Omega' + J_s(\vec{r}, \hat{s}) \tag{2.1}$$

where

- *I is the intensity.* The intensity is related to the power per unit solid angle and has the units of $\mathrm{W} \cdot \mathrm{m}^{-2} sr^{-1}$ for the case of the incident intensity while the scattered intensity

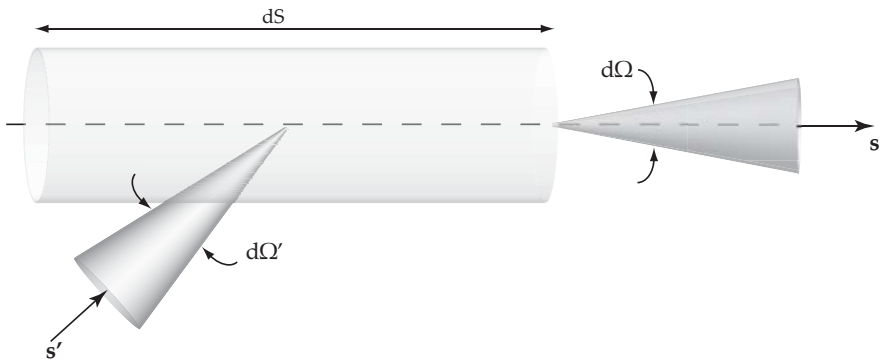

Figure 2.1: Basic geometry for Radiative Transfer Theory. Adapted from [Ishimaru, 1997].

has units of $\mathrm{W} \cdot \mathrm{m}^{-2}\mathrm{sr}^{-1}$ to account for radiation out of a volume element.

- *P is the Phase function*[1]. The Phase function describes the portion of the incident intensity scattered into the desired direction from an out-of-plane direction.
- *σ is the extinction coefficient.* The extinction coefficient accounts for the attenuation into the layer from both the scattering and the absorption of the power by the scattering elements. This can also be thought of as the sum of the absorption coefficient, σ_a, and the scattering coefficient, σ_s where $\sigma_t = \sigma_s + \sigma_a$.
- *J is the source function.* The source function represents the "self-emission" of the particles. This is the source of the observed power in passive remote sensing.

The above equation, (2.1), is the scalar Radiative Transfer equation, or SRTE. This equation is only applicable when the incident and scattered polarization are the same; i.e. vertical transmit - vertical receive (VV) or horizontal transmit - horizontal receive (HH). It is generally more applicable to reformulate this equation into a matrix expression which accounts for VV, HH, and cross polarization effects (VH/HV).

Graphically, this can be seen in Fig. 2.1. If an intensity, $I(\vec{r}, \hat{s})$, is incident on an increment volume element dS, containing ρ scattering elements per unit volume, there will be a decrease in the coherent intensity magnitude as a result of the absorption (σ_a) and scattering (σ_s) away from the direction of propagation, $\hat{s}$. On the other hand, the intensity will *increase* as a result of into-the-plane scattering from direction $\hat{s}'$. All into-plane scattering can be accounted for by integrating over the phase matrix, as shown in (2.1) [Ishimaru, 1997]. Thereby, Radiative Transfer Theory relies on the conservation of power through a random media.

[1]The term 'Phase' originated from the RTE use in astronomy and refers to the phases of the moon. It has no relation to the 'phase' of electromagnetic fields, as the RTE is formed based on incoherent scattering.

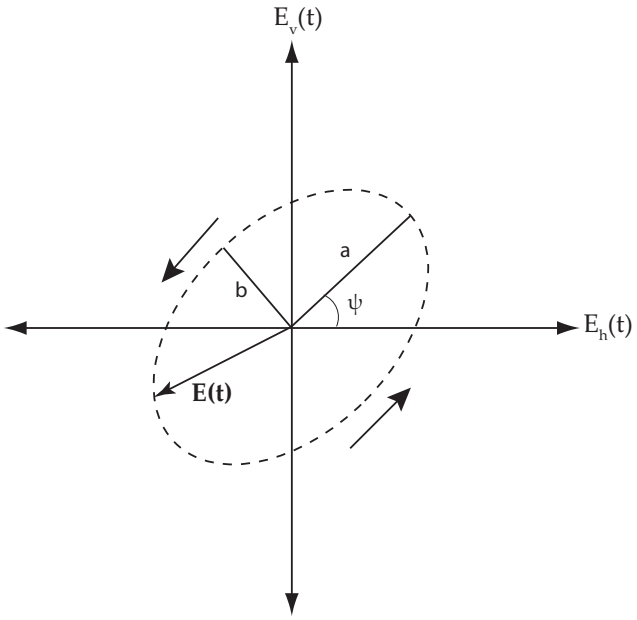

Figure 2.2: Elliptically-polarized electric field.

2.2 Stokes parameters and polarization

In order to express the Radiative Transfer equation given by (2.1) in terms of a polarized electric field, the Stokes parameters needs to be introduced [Ishimaru, 1991]. The Stokes parameters holds the advantages that the phase, amplitude and polarization of an arbitrary wave can always be described by the resulting matrix. Also, all quantities of the Stokes parameters can be physically measured.

First, consider an elliptically polarized electric field, as shown in Fig. 2.2. Assuming a time dependence of $e^{-j\omega t}$ [2], the electric field can be described as the sum of two orthogonal polarization components

$$\vec{E} = \vec{E}_v\hat{v} + \vec{E}_h\hat{h} \longleftrightarrow E(t) = a_1\cos(\tau + \delta_1)\hat{v} + a_2\cos(\tau + \delta_2)\hat{h} \tag{2.2}$$

where v and h represent vertical and horizontal, respectively, and $\tau = \omega t - kz$. The electric field traces out an ellipse described by

$$\left(\frac{E_v}{a_1}\right)^2 + \left(\frac{E_h}{a_2}\right)^2 - 2\frac{E_vE_h}{a_1a_2}\cos(\delta_2 - \delta_1) = \sin^2(\delta_2 - \delta_1). \tag{2.3}$$

[2]This time dependence is used in order to be consistent with most Radiative Transfer literature.

In order to mathematically describe such a wave, three independent quantities need to be given; typically the respective amplitudes and the phase difference. However, by defining a vector I such that

$$\mathbf{I} = \begin{bmatrix} I \\ Q \\ U \\ V \end{bmatrix} = \frac{1}{\eta} \begin{bmatrix} a_1^2 + a_2^2 \\ a_1^2 - a_2^2 \\ 2a_1 a_2 \cos(\delta_2 - \delta_1) \\ \mp 2_a 1 a_2 \sin(\delta_2 - \delta_1) \end{bmatrix} = \frac{1}{\eta} \begin{bmatrix} |E_v|^2 + |E_h|^2 \\ |E_v|^2 - |E_h|^2 \\ 2\Re\{E_v E_h^*\} \\ 2\Im\{E_v E_h^*\} \end{bmatrix} \tag{2.4}$$

where η is the intrinsic impedance of the background media, and the matrix elements are related to each other by

$$I^2 = Q^2 + U^2 + V^2, \tag{2.5}$$

it is seen that (2.5) and (2.4) completely define the ellipse. Furthermore, I, Q, U, and V all have the same units. The matrix elements of (2.4) are known as the Stokes parameters, named for the man who first "discovered" them, G.G. Stokes.

In Radiative Transfer Theory, it is more common to use the *modified* Stokes parameters defined as

$$\mathbf{I} = \begin{bmatrix} I_v \\ I_h \\ U \\ V \end{bmatrix} = \frac{1}{\eta} \begin{bmatrix} |E_v|^2 \\ |E_h|^2 \\ 2\Re\{E_v E_h^*\} \\ 2\Im\{E_v E_h^*\} \end{bmatrix} \tag{2.6}$$

and related through the Stokes condition

$$I^2 \geq Q^2 + U^2 + V^2. \tag{2.7}$$

The modified Stokes parameters are generally chosen for use in radiative transfer problems due to the separation of the intensity into the horizontal and vertical components. From here out, any reference to the "Stokes parameters" will assume the modified Stokes parameters.

2.3 Scattering from a Discrete Object

Consider an arbitrarily polarized electric field incident on a scattering element, as shown in figure Fig. 2.4. If the distance from the point of observation to the scattering element, R, is much greater than the average particle size, $< D >$, the near-field scattering can be ignored and only the far-field effects considered. If we assume the incident wave contains both a horizontally and vertically polarized component, the resultant scattered wave can be related

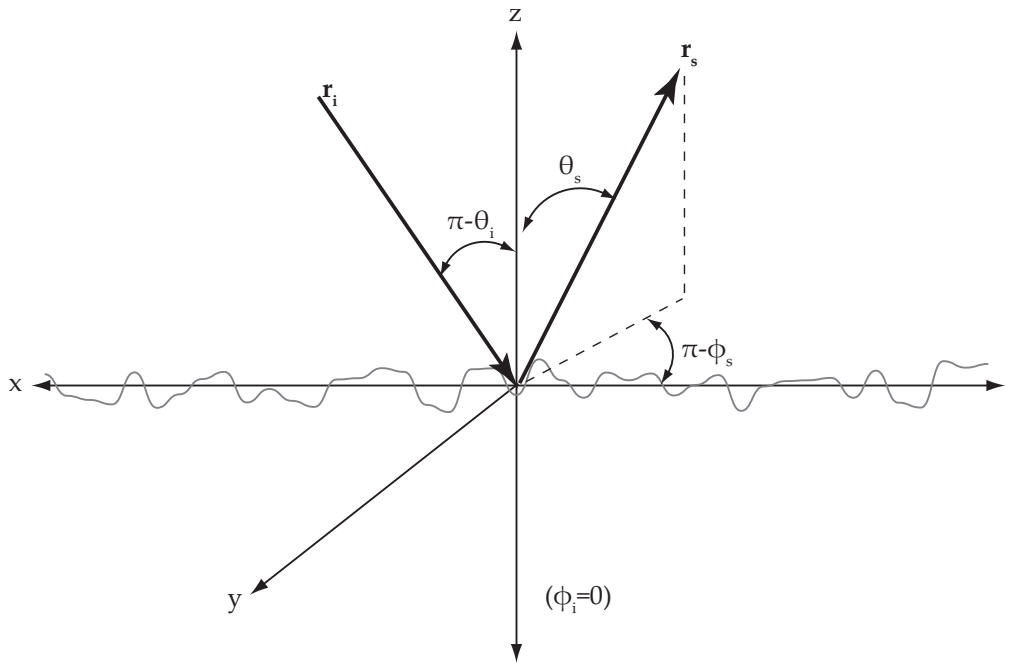

Figure 2.3: Coordinate system used for Radiative Transfer problems for an incident and reflected intensity from an arbitrary boundary ($\phi_i = 0°$).

to the incident wave via the scattering amplitude matrix, **F**, by the expression

$$\begin{bmatrix} E_v^s \\ E_h^s \end{bmatrix} = \frac{e^{+jkr}}{R} \begin{bmatrix} f_{vv} & f_{vh} \\ f_{hv} & f_{hh} \end{bmatrix} \begin{bmatrix} E_v^i \\ E_h^i \end{bmatrix} \tag{2.8}$$

where the scattering matrix element f_{mn} accounts for an $m-$ polarized scattered wave component resulting from an $n-$ polarized incident component. The exponential coefficient results from the Green's function for spherical waves. In general, all the components comprising the **F** matrix are functions of the incident (θ_i,ϕ_i) and scattered (θ_s,ϕ_s) angles, as shown in Fig. 2.3.

Using the above expression for the incident and scattered field, it is possible now possible to relate the corresponding incident and reflected intensities. The derivation is straightforward yet non-trivial, and only the steps will be outlined:

1. Using the Modified Stokes parameters (2.6), each element of the Stokes parameter vector is set equal to its corresponding incident electric field term from the expansion of (2.8).
2. The incident electric fields are rewritten in terms of the incident modified Stokes pa-

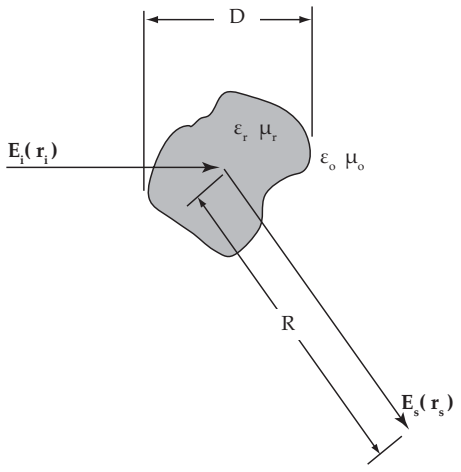

Figure 2.4: Incident and scattered E- field from a random dielectric particle.

rameters.

3. The 4x1 incident modified Stokes parameter vector is factored out resulting in the 4x4 Stokes (or Mueller) matrix, **L**.

Following these steps results in the 4x4 matrix Stokes matrix, **L**, which relates the incident and scattered intensities by[3]

$$\mathbf{I}_s = \frac{1}{R^2}\mathbf{L}\mathbf{I}_i.$$

Based on the general form of the above equation, it is seen that an incident plane wave on a scatterer, represented by I_i, results in a spherical reflected wave. This is to be expected as in order to add power levels incoherently, the scatterers must be in the far-field. In the far-field, the scatterer will reduce to a point, and therefore any scattered wave will attenuate as a spherical wave.

The expression for **L** is given by

$$\mathbf{L} = \begin{bmatrix} |f_{vv}|^2 & |F_{vh}|^2 & \Re\{f_{vv}f_{vh}^*\} & -\Im\{f_{vv}f_{vh}^*\} \\ |f_{hv}|^2 & |F_{hh}|^2 & \Re\{f_{hv}f_{hh}^*\} & -\Im\{f_{hv}f_{hh}^*\} \\ 2\Re\{f_{vv}f_{hv}^*\} & 2\Re\{f_{vh}f_{hh}^*\} & \Re\{f_{vv}f_{hh}^* + f_{vh}f_{hv}^*\} & -\Im\{f_{vv}f_{hh}^* + f_{vh}f_{hv}^*\} \\ 2\Re\{f_{vv}f_{hv}^*\} & 2\Re\{f_{vh}f_{hh}^*\} & \Re\{f_{vv}f_{hh}^* + f_{vh}f_{hv}^*\} & -\Im\{f_{vv}f_{hh}^* + f_{vh}f_{hv}^*\} \end{bmatrix} \tag{2.9}$$

which can be found in [Ishimaru and Yeh, 1984] along with a more complete derivation. Again, because the **F** matrix is a function of the incident and scattered angles, the Stokes vector is as well.

[3]Certain authors may include the R^{-2} term as part of the Stokes matrix or vector.

2.3.1 Euler Rotation of the Scattering Amplitude Matrix

As Radiative Transfer Theory relies on random scattering, it is often necessary to examine how a rotation of the scattering object affects the scattering amplitude matrix of (2.8). To do so, the object's scattering matrix is defined in terms of the local axis frame, denoted by the "prime" superscript (x', y', z'). These axis are rotated off of the main reference axis (x, y, z) by the Eulerian angles (α, β, γ) [Arfken, 1985]

$$\begin{bmatrix} x' \\ y' \\ z' \end{bmatrix} =$$
$$\begin{bmatrix} \cos\gamma\cos\beta\cos\alpha - \sin\gamma\sin\alpha & \cos\gamma\cos\beta\sin\alpha + \sin\gamma\cos\alpha & -\cos\gamma\sin\beta \\ -\sin\gamma\cos\beta\cos\alpha - \cos\gamma\sin\alpha & -\sin\gamma\cos\beta\sin\alpha + \cos\gamma\cos\alpha & \sin\gamma\sin\beta \\ \sin\beta\cos\alpha & \sin\beta\sin\alpha & \cos\beta \end{bmatrix} \times \begin{bmatrix} x \\ y \\ z \end{bmatrix}.$$

Following the work of [Karam and Fung, 1989], the polarization vectors, $\hat{v}/\hat{h}$, and incident and scattered vectors, $\hat{r}_{i/s}$, can also be expressed in both the local and reference coordinate systems. If $\mathbf{F}'$ is the scattering amplitude matrix in the local frame defined as the tensor,

$$\mathbf{F}' = \sum_{p',q'} F'_{pq} \hat{p}' \hat{q}'$$

it can be related to the scattering amplitude matrix in the reference frame by

$$\mathbf{F} = \sum_{p',q'} \hat{p} \cdot \mathbf{F}' \cdot \hat{q},$$

where p/q can be either v or h. Explicit expressions for these vectors in each coordinate frame can be found in [Karam and Fung, 1989].

2.4 The Vector Radiative Transfer Equation

To extend the Scalar Radiative Transfer Equation (SRTE) described in Section 2.1 into a vector expression accounting for polarization effects, the intensity, I is first replaced by the 4x1 Stokes parameters, $\mathbf{I}$. Consequently, the remaining terms, σ_t and p, need to be formulated into 4x4 matrices.

Next, recall that the Stokes Matrix of (2.9) represents the the relationship between the

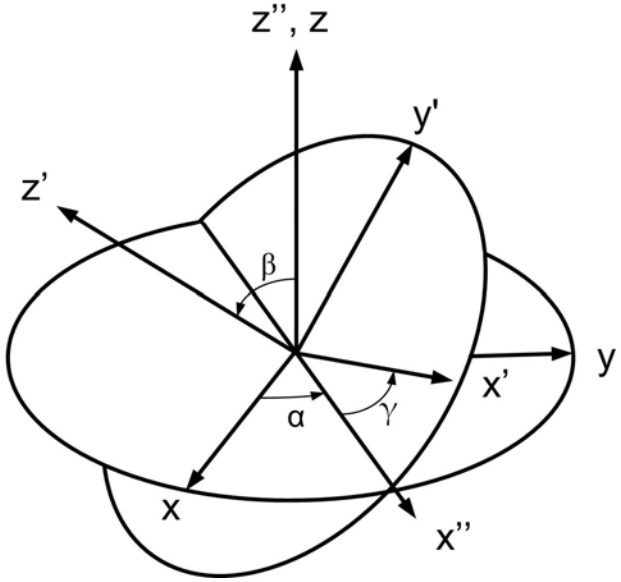

Figure 2.5: Euler axis of rotation. Adapted from [Rahmat-Samii, 1979]

incident and scattered intensities from a *single* scattering element. To expand this quantity to a volume region of scatterers, the Stokes matrix can simply be multiplied by the density of scatterers in the volume of interest, ρ. In doing so, however, the new Phase Matrix, $\mathbf{P}$, is now restricted to a layer of scatterers, each with with an orientation. In most applications, however, the scatterers will not be identically oriented, rather their orientation will have some degree of randomness to it. If the scatterers' orientation in a given volume can be described by a probability density function (pdf), then the Phase matrix can be further described as

$$\mathbf{P} = \rho \iiint \mathbf{L}(\alpha, \beta, \gamma)\mathrm{PDF}(\alpha, \beta, \gamma)\partial\alpha\partial\beta\partial\gamma \tag{2.10}$$

where from probability theory, the result of the integral is the $\mathbf{L}$ matrix averaged over scatterer orientation. Consequently, this term can also be written as

$$\mathbf{P} = \rho \langle \mathbf{L} \rangle$$

where the brackets denote the average over the angles of orientation. What this indicates is that the phase matrix can be thought of as the Stokes matrix per unit volume.

To account for the attenuation of the polarized wave, an extinction matrix, κ is introduced. Following the derivation outlined in [Ishimaru and Cheung, 1980] [Ishimaru and Yeh, 1984],

the extinction matrix is related to the **F** matrix by

$$\kappa_e = \begin{bmatrix} -2\Re\{M_{vv}\} & 0 & -\Re\{M_{vh}\} & -\Im\{M_{vh}\} \\ 0 & -2\Re\{M_{hh}\} & -\Re\{M_{hv}\} & \Im\{M_{hv}\} \\ -2\Re\{M_{hv}\} & -2\Re\{M_{vh}\} & -[\Re\{M_{vv}\}+\Re\{M_{hh}\}] & \Im\{M_{vv}\}-\Im\{M_{hh}\} \\ 2\Im\{M_{hv}\} & -2\Im\{M_{vh}\} & -]\Im\{M_{vv}\}-\Im\{M_{hh}\}] & -[\Re\{M_{vv}\}+\Re\{M_{hh}\}] \end{bmatrix} \tag{2.11}$$

where

$$M_{mn} = \frac{j2\pi\rho}{k_o}\left\langle f_{mn}(\hat{r}_i, \hat{r}_s)\right\rangle$$

and the brackets again denote the averaging over the orientation of the scatterer population.

By replacing the scalar phase-, extinction-, and intensity- functions with their matrix counterparts, the SRTE can now be replaced by the Vector Radiative Transfer Equation (VRTE),

$$\frac{\partial}{\partial s}\mathbf{I}(r,s) = -\kappa_e(s,r)\mathbf{I}(s,r) + \iint_{4\pi}\mathbf{PI}(r,s)d\Omega + J_s. \tag{2.12}$$

It should be noted that in order to conserve units, the scattered intensity, located in the integral, is generally assumed to be normalized by the unit solid angle, $d\Omega = A\cos\theta_s/r^2$.

2.4.1 Special Case of the VRTE

It is now helpful to investigate how the VRTE of (2.12) applies to cases were a random volume may contain multiple "families" of scatterers. As only the incoherent propagation is dealt with in Radiative Transfer theory, it can be assumed that the elements of a given "family" will scatter any propagating wave independently of the other scattering families. Therefore the total phase and extinction matrices for a given medium containing N distinct families of scatterers is merely the sum of the extinction and phase matrices of the individual families, or

$$\kappa_{total} = \sum_{n=1}^{N}\kappa_n$$
$$\mathbf{P}_{total} = \sum_{n=1}^{N}\rho_n\left\langle\mathbf{L}_n\right\rangle.$$

For example, if a given volume contains both spherical and cylindrical scattering objects, then the κ for the total volume would be the sum of the individual κ for the spheres and cylinders. The same additive property also applies to the phase matrix.

2.5 Solution to the Transfer Equations

As written in (2.12), there exists no purely analytical solution to the Radiative Transfer equation. As a result, authors have taken various approaches to solving this equation; with the two most notable being an iterative solution and a geometrical dependent solution. The geometrical solution is considered "exact", however, it relies on symmetry in the phase matrix which will only occur when the medium contains *only* purely spherical scatterers. Other approaches rely on purely numerical techniques. However, these approaches offer little physical insight to what interactions within the random media are contributing to the overall propagation and scattering. Consequently, this thesis will focus on the more general but slightly more restricted iterative approach.

To solve the VRTE iteratively, the intensity is broken into two coupled equations. The upwelling component,

$$\frac{d}{dz}I_n^+(\mu,\phi,z) = -\frac{1}{\mu}\kappa_n I_n^+(\mu,\phi,z)+ \frac{1}{\mu}\iint\limits_{4\pi} P_n(\mu,\phi;\mu_i,\phi_i)I_n^+(\mu_i,\phi_i,z)\,d\Omega'+ \frac{1}{\mu}\iint\limits_{4\pi} P_n(\mu,\phi;\mu_i,\phi_i)I_n^-(\mu_i,\phi_i,z)\,d\Omega'$$

and downwelling component,

$$-\frac{d}{dz}I_n^-(-\mu,\phi,z) = -\frac{1}{\mu}\kappa_n I_n^-(-\mu,\phi,z)+ \frac{1}{\mu}\iint\limits_{4\pi} P_n(-\mu,\phi;\mu_i,\phi_i)I_n^+(\mu_i,\phi_i,z)\,d\Omega'+ \frac{1}{\mu}\iint\limits_{4\pi} P_n(-\mu,\phi;\mu_i,\phi_i)I_n^-(-\mu_i,\phi_i,z)\,d\Omega',$$

where it is assumed that the upwelling component will not contribute to the downwelling component and $\mu = \cos\theta$. This is an accurate assumption when dealing with foliage media. The source component, J_s, has also been omitted do to its negligible effect when dealing with active remote sensing [Ulaby et al., 1990].

From the general formulation of RT theory as outlined in §2.1, it is evident that the κI term represents the attenuation of the coherent wave as it propagates through the medium, while

the integral terms represent the "in-plane" scattering. These terms can then be grouped of as "source terms", S, and the corresponding up-/down- welling intensities expressed as

$$\frac{d}{dz}I_n^+(\mu,\phi,z) = -\frac{1}{\mu}\kappa_n I_n^+(\mu,\phi,z) + S(\mu,\phi,z) \tag{2.13}$$

$$-\frac{d}{dz}I_n^-(-\mu,\phi,z) = -\frac{1}{\mu}\kappa_n I_n^-(-\mu,\phi,z) + S(-\mu,\phi,z) \tag{2.14}$$

where S can be inferred from the previous definitions of the traveling intensities [Karam et al., 1992].

By changing the the differential equations to integral equations, (2.13) and (2.14) become [Ulaby et al., 1986]

$$I_n^+(z) = e^{-\kappa_n(z+d)/\mu}I_n^+(\mu,\phi,-d) + \int_{-d}^{z} e^{-\kappa(z-z')/\mu}S(\mu,\phi,z')dz' \tag{2.15}$$

$$I_n^-(z) = e^{-\kappa_n(z)/\mu}I_n^+(-\mu,\phi,0) + \int_{z}^{0} e^{-\kappa(z-z')/\mu}S(-\mu,\phi,z')dz'. \tag{2.16}$$

Using the above equations, it is then possible to derive an iterative scheme to solve for the upward and downward traveling intensities. The solution itself depends on several factors including the number of layers and the boundary conditions at each layer interface. However, the general iterative procedure for the solution of (2.15) and (2.16) is as follows:

1. **Determine the boundary conditions.** For propagation in a given layer, an upper and lower boundary condition is needed for both the upwelling and down welling intensities. The boundary conditions are generally vectors describing the intensities at the interfaces traveling in the specified direction. Therefore, boundary conditions are generally the value of the intensities from a bordering layer, or, in the case of reflective boundaries, an incident Stokes vector multiplied by some reflectivity matrix.

2. **Find the zeroth order solution.** The zeroth order solution is found by setting the source terms to zero. Physically, this represents a wave propagating through the layer and consequently being attenuated via scattering and absorption. All contributions of "additive" scattering are ignored.

3. **Iterate the solutions.** Once a zeroth order solution is found, this term is treated as the source term in (2.15) and (2.16) in order to find the first order solution to the problem. Second order terms are then found by using the first order solution as the source term, etc, until the desired order is obtained.

The result of the preceding steps is a series of terms, each of which will represent a physical scattering path. For example, a first order solution will account for "single-bounce" interactions within a given layer. A second order solution will account for "double-bounces" in a given layer, etc.

2.6 Limits of Radiative Transfer Theory and the Iterative Solution

Radiative Transfer Theory contains several limiting factors that affect its applicability to common remote sensing applications. Most limits are directly or indirectly related to the density of scatterers per unit volume. First, the Radiative Transfer solution has been found to only be accurate when the fractional volume of the scatterers is 1% or less [Ulaby and Elachi, 1990]. In order to incoherently add the intensities, the assumption was made that there were no "near-field" interactions between scatterer particles. This assumption is valid for sparse medium. However, in dense medium, the scatterers will inevitably be located in each others' near-field, thereby causing coherent interactions not accounted for in common Radiative Transfer Theory.

One important example in which the coherent additions and multiple scatterings associated with higher densities play an important role in is the phenomena known as backscatter enhancement [Tsang et al., 1985]. It has long been observed that the backscatter cross section of dense random volumes contains a sharp peak in the backscatter direction. This can be attributed to the coherent additions of higher-order scattering terms. Recall that RT theory is based on the assumption that we may incoherently add power levels. For example, consider a second order scattering problem in which an electromagnetic wave incident on a random volume scatters from a random Particle 1 to a random Particle 2 before returning to the surface as shown in Fig. 2.6(a) (E_{12}). There will also be present an inverse to this term, E_{21}. The total average power is therefore proportional to

$$< |E|^2 >=< |E_{21}|^2 > + < |E_{12}|^2 > +2\Re \left\{ E_{12} E_{21}^* \right\}.$$

The random positioning of the particles will result in a random phase difference, which, when averaged, is equal to zero. The resulting power, from reciprocity, is therefore

$$< |E|^2 >= 2 < |E_{21}|^2 >= 2 < |E_{12}|^2 >$$

The result is that the total power is the sum of the individual powers, as predicted in RT theory. However, in the case of backscattering, the phase difference between E_{21} and E_{12} vanishes and the two fields *become equal* (Fig. 2.6(b)). The result is a coherent addition,

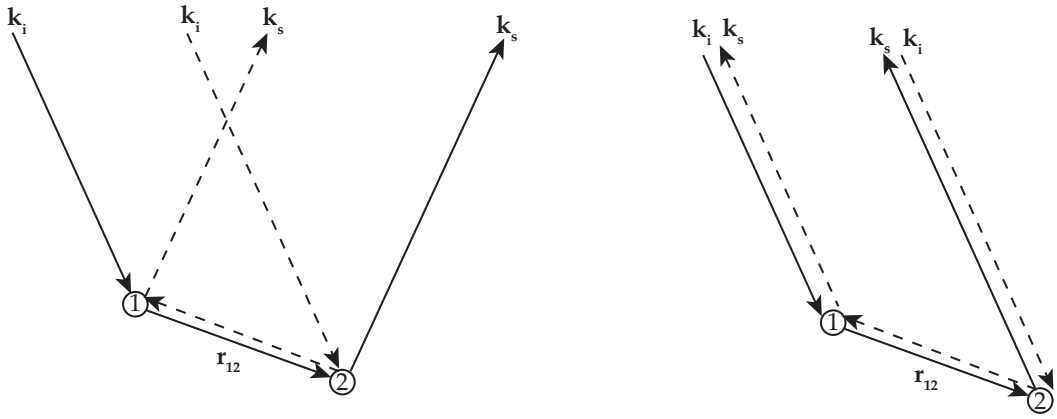

(a) (b)

Figure 2.6: Scattering paths for the (a) incoherent and (b) coherent additions. Adapted from [Tsang et al., 1985].

causing $\Re\{E_{12}E_{21}^*\} = 2 < |E_{12}|^2 >= 2 < |E_{21}|^2 >$ and

$$< |E|^2 >= 4 < |E_{21}|^2 >= 4 < |E_{12}|^2 >$$

thereby explaining the sharp increase experienced in the measured cross section of dense media in the backscatter direction. While the above explanation applies to the second order scattering, a similar derivation can be done for higher orders.

Another limitation arises from the assumption made in the iterative solution. Recall that in the iterative solution, the total intensity was decomposed into an upwelling and downwelling component, which were uncoupled. The zeroth order solution assumed that scattering contributed to an attenuation of the incident wave, but did not cause any "redirection" or out-of-plane effects. This term was then iterated upon and served as a starting point for all other orders of solutions. However, if the scattering process is not small compared to the absorption process, the upwelling wave would be directly coupled to the downwelling wave, and the iterative solution would be invalid.

The extent to which these limitations apply to remote sensing of foliage will be discussed in Chapter 3 along with the affect they may have on the model developed in this thesis [4].

[4] See §3.2.

Chapter 3

Remote Sensing and the VRTE

The most common solutions to the remote sensing problem generally revolve around the time-harmonic radiative transfer equations, outlined in Chapter 2. While full-wave simulations of foliage would yield ideal simulation results, the time necessary to implement and run such simulations is generally cost prohibitive. On the other hand, RT solutions are much faster to implement when dealing with random scattering regions and can be loosely tied into the underlying physics.

One of the most well established and extensive models is the Michigan Microwave Canopy Scattering Model, MIMICS [Ulaby et al., 1990]. Developed in the early 1990's at the University of Michigan, this model relies heavily on Radiative Transfer theory to estimate the backscatter from orchards and fields. Recent work has further developed MIMICS to account for the growing need of bistatic scatter models and multi-leveled models [Liang et al., 2005a] [Liang et al., 2005b].

This chapter will introduce and discuss the application of RT theory to remote sensing. The focus will be on the MIMICS solution, which will provide a solid, proven starting point for the model developed in later chapters. While initially the model centered around the original MIMICS solution of [Ulaby et al., 1990], during the course of this project, MIMICS was updated to the more general case of N- multiple layers [Liang et al., 2005b]. As the original case is merely a special case of the multi-layer model, any reference to MIMICS will refer to the multi-layer model.

Expressions used to model the random scatterers can be found in various literature and appear in Appendix B without derivations.

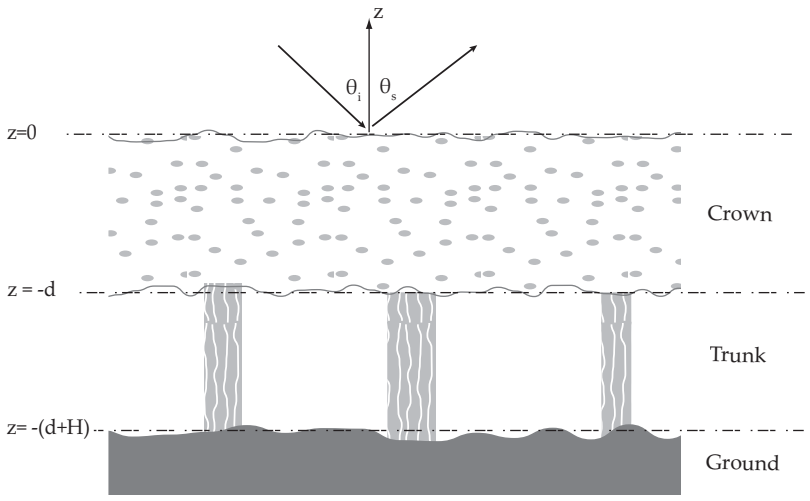

Figure 3.1: General model for foliage and trunk layers above ground (N = 2 Layers).

3.1 Model Geometry

To begin with, the vegetation is generally divided into separate layers. Traditional approaches such as those found in [Ulaby et al., 1990] and [Karam et al., 1992] do so by creating a foliage layer and a trunk layer, as well as some sort of underlying ground, generally either specular or quasi-specular (Fig. 3.1).

These models generally account for

1. Surface roughness via a correction factor or small perturbation technique.
2. Volume scattering from the crown and trunk layers.
3. First- or Second- order scattering involving ground-crown and ground-trunk interactions.

The necessary iteration of the VRTE solution is dependent on the frequency of operation. Measurements indicate that at X-band and lower, the dominating scattering terms are contained in the first order solution [Karam et al., 1992]. Remote sensing of foliage above X-band, may require the use of second order terms, depending on various statistics of the foliage. However, a comprehensive limit for the first order solution has never been truly determined.

Most, if not all, models consist of diffuse boundaries between each layer, with the exception of any dielectric earth. Each trunk or crown layer has homogeneous statistics in the $\hat{x}$ and

$\hat{y}$ directions.

3.2 The Crown Layer

In order to define the crown layer, its underlying volume elements are first defined. Generally, the crown is assumed to consist of (1) leaves modeled as dielectric discs or sheets, (2) needles modeled by thin, elongated dielectric spheroids, and/or (3) branches modeled by dielectric cylinders. These elements are again dependent on the type of vegetation being modeled: with needles and cylinders suitable for modeling the needles and branches of coniferous vegetation; and discs, sheets, and cylinders suitable for modeling the leaves and branches of deciduous vegetation. To incorporate these quantities into the VRTE problem, the radiated field is solved for each of the elemental scatterers. This can either be done analytically, as is the case for [Karam et al., 1988] or through a simulation code such as the Method of Moments.

More recently, various authors have chosen to implement multi-layered crown models to better account for changes in the constituent scattering elements; such as changes in their orientation, and various density gradients observed in the canopy profile (Fig. 3.2) [Liang et al., 2005b]. While the original MIMICS and corresponding models were successful at simulating backscatter from well-maintained orchards and commercial crop fields, it remained relatively untested for more general forest situations. With the introduction of multiple layers, it has become much easier to model more general "mixed-species" forests where the height statistics of the crown layer may not easily conform to a single layer.

The dominating back scattering mechanism in the crown layer(s) is most commonly a single, direct backscatter from the foliage. Foliage-foliage backscattering is generally negligible at most frequencies of interest, due particularly to the fact that if this mechanism was dominant, the signal would not be able to propagate very deeply into the vegetation, thereby providing little information to the observer. Furthermore, at higher frequencies, the absorption loss will also increase, again clouding the extraction of useful information from the return. *Because the higher-order interactions are negligible over the frequencies of interest in the remote sensing of vegetation, the effect of backscatter enhancement as discussed in §2.6 is generally negligible. This also provides a good indication that the iterative solution to the VRTE is an acceptable one.*

In practice, many different scattering elements can be, and are, implemented in various foliage scattering models. One of the most widely used and successful scatterer used is the dielectric circular disc. The disc provides a good analogy to the deciduous leaf. If a closed form expression is needed, the scattering matrix of (2.8) can be derived using three different methods, each with their own regions of validity. First, the Rayleigh approximation assumes

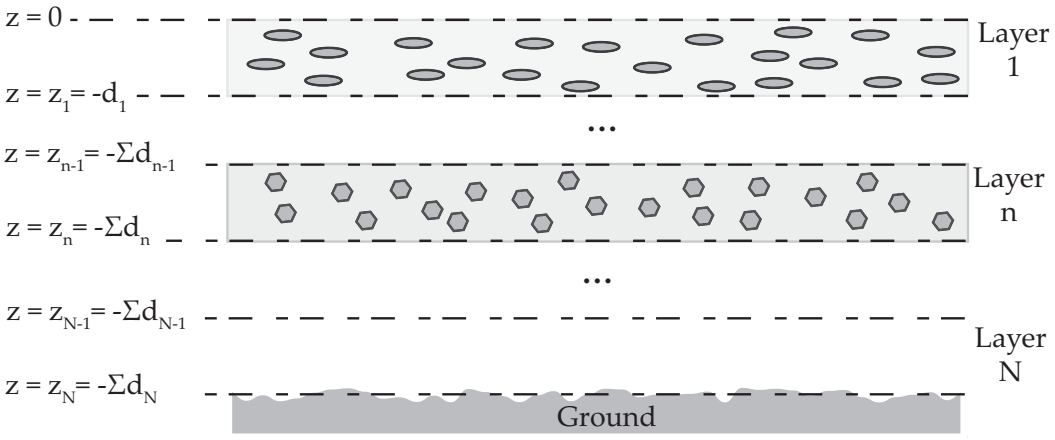

Figure 3.2: Dimensions for multilayer canopy model.

a uniform field inside the object [Karam and Fung, 1983]. The result is a very limited model, applicable only to situations in which all dimensions of the object are much less than a wavelength. As a Rayleigh approximation will lead to a more isotropic scatter pattern, it is evident that this may violate assumptions in the iterative solution which primarily accounts for forward and backward scattering, Furthermore, it is unlikely that a crown layer will consist only of particles and leaves much smaller than a wavelength. While an unlikely candidate for foliage scattering, this approximation has been applied with success to scattering from rain cells. Next, the Rayleigh-Gans approximation can be used which provides a correction factor, yet still is only valid for tenuous scatterers. In general, this provides a good approximation from coniferous foliage by modeling thin needles. Finally, the generalized Rayleigh-Gans (GRG) approximation can be used which modifies the previous method's solution by a Debye interference function. Using the GRG approach, the only limiting constraint of the scatterers dimension is that at least 1 dimension be much smaller than a wavelength. This proves to be very useful in modeling foliage, as many leaves may have widths and lengths on the order of a wavelength, but very thin depths. Using the GRG circular disc, the backscatter cross section is seen in Fig. 3.3 for a single element [Karam and Fung, 1989].

Models are also present which calculate the estimated dielectric constant of the simulated leaves and branches. The most common model used to calculate the dielectric constant of geophysical media is discussed in [Ulaby and El Rayes, 1987]. The model relies on a quasi-empirical formula which accounts for the vegetations' gravimetric moisture content, m_g.

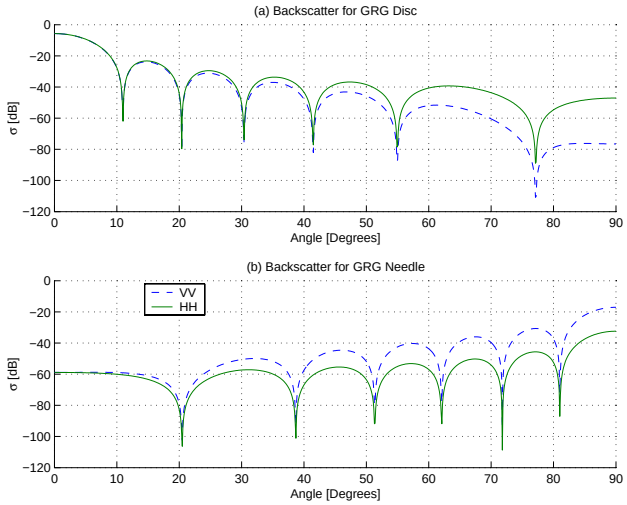

Figure 3.3: Backscatter from (a) circular disc of $a = 5.0cm$, $2h = 0.2mm$, and (b) needle of $h =$, $a =$, with $\epsilon_r = 28.04 - j13.34$ calculate by applying the generalized Rayleigh-Gans (GRG) formulation.

3.3 The Trunk Layer

The trunk layer for most forest models generally consists of near-vertical dielectric cylinders. In early static 2 layer models, the trunk layer was explicitly defined. However, as the usage of N- layer models has increased, the trunk layer is often treated as simply the N^{th} layer.

The trunk layer return, unlike the crown layers, generally has a negligible direct backscatter term. The reason being most trunk layers in nature consist of near vertical cylinders, the scattering from which roughly appears to be specular. Therefore, with the exception of low-grazing angle incidence, the direct backscatter from these objects is negligible. While the direct backscatter is negligible and can often be ignored, interactions between the ground and the trunk may have a dominating effect on the radar return. For the case of near vertical cylinders and a specular ground, the two layers form an approximate 90° corner reflector, with a well known behavior in the backscatter region (Fig. 3.4). For an $h-$ polarized incident wave[1], the ground-trunk interaction is expected (and observed) to be very large and may be the most dominant form of backscatter in the entire model. On the other hand, a $v-$ polarized incidence will most likely have very weak ground-trunk backscatter and therefore the trunk layer as a whole will have very little effect on the overall backscatter coefficient.

[1]E- field polarized in the $\hat{y}-$ direction in accordance with Fig. 2.3.

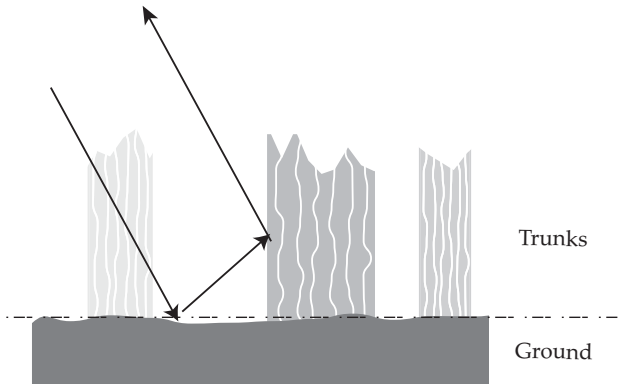

Figure 3.4: Corner reflector formed by trunk-ground interaction.

3.4 The Ground Layer

The ground layer for VRTE remote sensing models is a relatively gray area, with no unified solution. In the case of a specular ground, It can be shown that the incident Stokes vector can be related to the reflected Stokes vector through the relationship

$$\Gamma(\theta) = \begin{bmatrix} |\gamma_v(\theta)|^2 & 0 & 0 & 0 \\ 0 & |\gamma_h(\theta)|^2 & 0 & 0 \\ 0 & 0 & \Re\{\gamma_v(\theta)\gamma_h^*(\theta)\} & -\Im\{\gamma_v(\theta)\gamma_h^*(\theta)\} \\ 0 & 0 & \Im\{\gamma_v(\theta)\gamma_h^*(\theta)\} & \Re\{\gamma_v(\theta)\gamma_h^*(\theta)\} \end{bmatrix} \tag{3.1}$$

which was derived from Snell's Law and $\gamma_{v/h}$ is the Fresnel reflection coefficient for vertical or horizontal polarizations [2] [Tsang et al., 1985].

However, as a purely specular ground is rarely if ever encountered in remote sensing applications, various methods have been employed to account for rough surfaces. Ulaby et al treat the ground as specular when dealing with ground-crown interactions and introduce an additional term to account for non-specular backscatter from a rough surface [Ulaby et al., 1990]. Karam et al. account for the rough ground - crown interactions by performing an integration over a bistatic scattering coefficient for the rough surface. While the latter would inevitably yield more accurate results, the integration over the scattering coefficient comes at the cost of increased complexity and computation time. Both methods have been field tested with success. As many grounds are quasi-specular in nature, unless a radar is operated at nadir incidence, the ground will only affect the overall backscatter coefficient through an

[2] Consequently, a similar matrix can also be derived to relate the incident to transmitted Stokes vector across a dielectric medium.

interaction with the trunk or foliage.

If a rough surface correction factor is used, a 4x4 matrix can be constructed which accounts for the bistatically scattered intensity and is generally represented by $G(\mu, \phi, \mu_i, \phi_i)$. This matrix itself can be constructed a number of different ways depending on the roughness of the surface. Generally, a quasi-stationary or physical optics approach is used to model the ground and the equivalent parameters extracted. One such approach, outlined in [Lam and Ishimaru, 1994], use the Kirchoff approximation for rough surfaces to model the average reflectivity matrix for a Gaussian rough surface. The Kirchhoff approximation is only valid for very slowly varying surfaces. As a result, the scattering in the specular direction is largest, surrounded by a very low diffuse scattering in all other directions. For a slightly rough surface, a specular ground approach has been shown to be a good first order estimate for most remote sensing problems [Ulaby et al., 1990].

3.5 The MIMICS Solution for 1^{st} Order Backscatter

The MIMICS Solution to the VRTE problem follows the multi-layer structure of Fig. 3.2. The VRTE of (2.12) is solved iteratively following §2.5. A complete set of derivations and explanations can be found in [Liang et al., 2005b], as only the main points are outlined here. The solution seeks to obtain a matrix, referred to as the transformation matrix, which relates an incident plane wave to a scattered spherical wave by

$$\mathbf{I}_s = \mathbf{T}\mathbf{I}_i. \tag{3.2}$$

where $\mathbf{I}_{s/i}$ are scattered spherical and incident planar waves described by Stokes parameters. Explicitly written,

$$\mathbf{I}_i = \begin{bmatrix} I_v \\ I_h \\ U \\ V \end{bmatrix} = \frac{1}{\eta} \begin{bmatrix} |E_v^i|^2 \\ |E_h^i|^2 \\ 2\Re\{E_v^i E_h^{i*}\} \\ 2\Im\{E_v^i E_h^{i*}\} \end{bmatrix}$$

and

$$\mathbf{I}_s = \begin{bmatrix} I_v \\ I_h \\ U \\ V \end{bmatrix} = \frac{r^2}{\eta A \cos\theta_s} \begin{bmatrix} < |E_v^s| >^2 \\ < |E_h^s| >^2 \\ 2\Re\{< E_v^s E_h^{s*} >\} \\ 2\Im\{< E_v^s E_h^{s*} >\} \end{bmatrix}.$$

where $<>$ is the average incoherent return and the $r^2/A\cos\theta_s$ factor arises from the normalization of the scattered field by the unit solid angle as required for distributed targets.

To begin with, the boundary conditions for the upward and downward traveling wave are

defined as follows

$$I_1^-(-\mu,\phi,0) = I_o^-(-\mu_i,\phi_i,0)\delta(\mu-\mu_i)\delta(\phi-\phi_i) \tag{3.3a}$$
$$I_n^i(-\mu,\phi,-z_n) = I_{n+1}^-(-\mu,\phi,-z_n) \tag{3.3b}$$
$$I_N^+(\mu,\phi,-z_L) = \Gamma(\mu)I_N^-(-\mu,\phi,-z_N) \tag{3.3c}$$
$$I_n^+(\mu,\phi,-z_n) = I_{n+1}^-(\mu,\phi,-z_n) \tag{3.3d}$$
$$I_s(\mu,\phi) = I_1^+(\mu,\phi,0). \tag{3.3e}$$

Solving these equations yields

$$T(\mu,\phi) = \sum_{n=1}^{N} T_{gng} + T_{ng} + T_{gn} + T_n + T_{rs} \tag{3.4}$$

where

$$T_{gng}(\mu,\phi) = \frac{1}{\mu}\left[\prod_1^N\right]\Gamma(\mu)\left[\prod_1^N\right]A_{gng}(\mu,\phi;\mu_i,\phi_i)\left[\prod_1^N\right]\Gamma(\mu_i)\left[\prod_1^N\right] \tag{3.5a}$$
$$T_{ng}(\mu,\phi) = \frac{1}{\mu}\left[\prod_1^N\right]\Gamma(\mu)\left[\prod_{n+1}^N\right]A_{ng}(\mu,\phi;\mu_i,\phi_i)\left[\prod_1^{n-1}\right] \tag{3.5b}$$
$$T_{gn}(\mu,\phi) = \frac{1}{\mu}\left[\prod_1^{n-1}\right]A_{gn}(\mu,\phi;\mu_i,\left[\prod_{n+1}^N\right]\Gamma(\mu_i)\left[\prod_1^N\right] \tag{3.5c}$$
$$T_n(\mu,\phi) = \frac{1}{\mu}\left[\prod_1^{n-1}\right]A_n(\mu,\phi;\mu_i,\phi_i)\left[\prod_1^{n-1}\right] \tag{3.5d}$$
$$T_{rs}(\mu,\phi) = \frac{1}{\mu}\left[\prod_1^N\right]G(\mu,\phi,-\mu_i,\phi_i)\left[\prod_1^N\right], \tag{3.5e}$$

Term	Description
T_{gng}	Propagation through the crown and trunk, specular reflection from the ground, propagation up through the trunk, backscatter from n^{th} layer, specular reflection from the ground, and propagation through the trunk and crown.
T_{gn}	Propagation through the crown and trunk, specular reflection from the ground, propagation up through the trunk, and scattering by the crown.
T_{ng}	The reciprocal path of T_gn.
T_n	Direct backscattering from the crown.
T_{rs}	Propagation through the crown and trunk layers, backscattering by *rough* surface and propagation back up through the trunk and crown layers.

Table 3.1: Scatter path descriptions for MIMICS Solution of Fig. 3.5.

and

$$A_{gng} = \int_{-z_n}^{-z_{n-1}} e^{-\kappa_n(z_n+z')/\mu} P_n(-\mu,\phi;\mu_i,\phi_i) e^{-\kappa_n(z'+z_n)/\mu_i} dz' \tag{3.6a}$$

$$A_{ng} = \int_{-z_n}^{-z_{n-1}} e^{-\kappa_n(z_n+z')/\mu} P_n(-\mu,\phi;-\mu_i,\phi_i) e^{+\kappa_n(z'+z_{n-1})/\mu_i} dz' \tag{3.6b}$$

$$A_{gn} = \int_{-z_n}^{-z_{n-1}} e^{+\kappa_n(z_{n-1}+z')/\mu} P_n(\mu,\phi;\mu_i,\phi_i) e^{-\kappa_n(z'+z_n)/\mu_i} dz' \tag{3.6c}$$

$$A_n = \int_{-z_n}^{-z_{n-1}} e^{+\kappa_n(z_{n-1}+z')/\mu} P_n(\mu,\phi;-\mu_i,\phi_i) e^{+\kappa_n(z'+z_{n-1})/\mu_i} dz'. \tag{3.6d}$$

In the above expressions the shorthand notation

$$\left[\prod_a^b\right] = \prod_{m=a}^{b} e^{-\kappa_m d_m/\mu}$$

was used. Each term in the above equation (3.4)-(3.5) corresponds to a specific scattering term described in Tab. 3.1 and illustrated in Fig. 3.5. Several conclusions can be drawn from this solution. First we see that first order solutions yield 4 scattering terms for each layer. The incoherent nature of the VRTE is what allows for the summation of the contributions from each individual layer. Each scattering term, T_i, contains (1) attenuation factors, represented by the exponential term, which represent the attenuation of the field as it is scattered and absorbed by the medium; and (2) a scattering term, A_i which accounts for scattering interactions from the incident direction into the observation direction.

It is also important to note that the first-order iterative approach combined with a specular

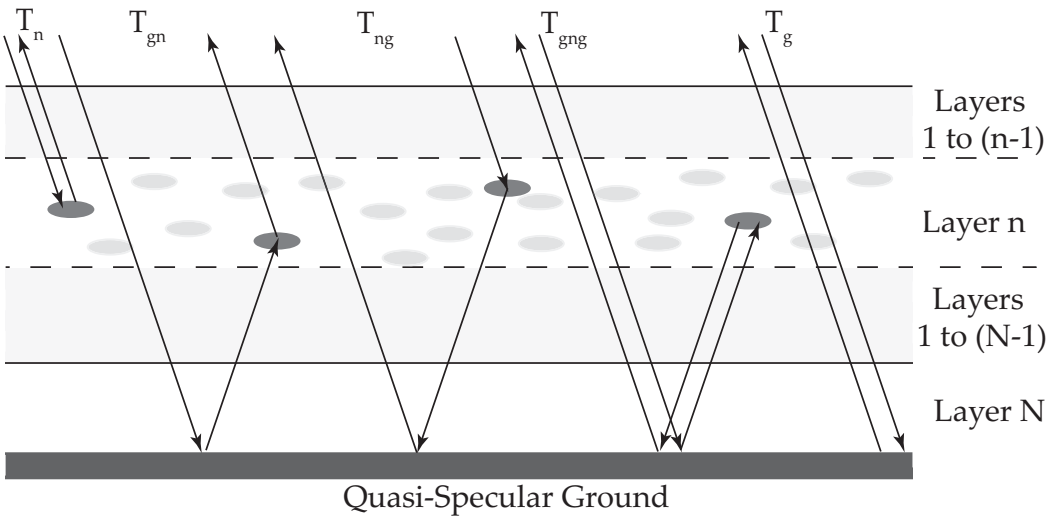

Figure 3.5: Scattering terms from iterative MIMICS Solution.

ground eliminates all integrations over the solid angle. This is a direct result of the "impulse" behavior of the boundary conditions.

3.6 Quantifying Remote Sensing Returns

From the transformation matrix, linear backscatter coefficients can be derived using the definitions of the incident and scattered intensities. The linear backscatter coefficient corresponding to a β polarized plane wave incident on an area, A, giving rise to an α polarized spherical wave is defined as

$$\sigma^o_{\alpha\beta} = \frac{4\pi r^2}{A} \frac{< |E^s_\alpha| >}{|E^i_\beta|} = 4\pi \cos\theta \frac{I^s_\alpha}{I^i_\beta} \tag{3.7}$$

where α/β can be $v-$ or $h-$ polarization. The angular dependence has been assumed, however, if $\hat{k}_i$ is the direction of propagation for the incident wave, then, in the case of backscattering, the direction of the scattered wave must be $-\hat{k}_i$.

Often it is more desirable calculate the *polarization signature* of the random media at the $z = 0$ surface, which is given by [Ishimaru, 1991]

$$\mathcal{P}_s = \mathbf{h}^{\mathrm{T}} \mathbf{T} \mathbf{I}_{tn} \tag{3.8}$$

where T is the transpose operator and $\mathbf{h}$ is the complex effective antenna height, given as

$$\mathbf{h} = \begin{bmatrix} \frac{1}{2}(1 + \cos 2\chi_r \cos 2\psi_r) \\ \frac{1}{2}(1 - \cos 2\chi_r \cos 2\psi_r) \\ -\frac{1}{2}\cos 2\chi_r \sin 2\psi_r \\ \frac{1}{2}\sin 2\chi_r \end{bmatrix} \tag{3.9}$$

which accounts for polarization matching between the receiving antenna and the EM wave incident on the receiving antenna. I_{tn} is the normalized incident intensity resultant from the transmitting antenna,

$$\mathbf{I}_{tn} = \begin{bmatrix} \frac{1}{2}(1 + \cos 2\chi_t \cos 2\psi_t) \\ \frac{1}{2}(1 - \cos 2\chi_t \cos 2\psi_t) \\ \cos 2\chi_t \sin 2\psi_t \\ \sin 2\chi_t \end{bmatrix}. \tag{3.10}$$

The angles $\chi_{r/t}$ and $\psi_{r/t}$ are the ellipticity and orientation angles, respectively, of the receiving/transmitting antenna. For the case of a monostatic radar in which the receive and transmit antenna are the same, $\chi_r = \chi_t$ and $\psi_r = \psi_t$ This in turn can be used to predict an arbitrary backscatter coefficient [Tsang and Ding, 1991]

$$\sigma^o = 4\pi \cos\theta_i \mathcal{P}_s. \tag{3.11}$$

It should be noted that extracting precise information about a target from its polarization signature is impossible, as the signatures from various terrains may not be distinct. This has lead various authors to refer to them therefore as *polarization responses* [Ulaby and Elachi, 1990]. Nonetheless, by examining the polarization signature of a given canopy over a period of time, the signatures can be used to empirically extract useful information such as moisture content, density, and the presence of targets.

3.7 Example: Spheres and Discs above a Dielectric Ground

In order to demonstrate the functionality of the VRTE model, the problem of a time-harmonic field incident upon a layer of spheres above a dielectric half-space will be considered. It is easiest to begin with the transformation matrix formulation described in §3.5. If we set the number of scattering layers to $N = 1$ we obtain a single layer transformation

matrix with four distinct terms

$$T(\mu_i, \phi_i + \pi; \mu_i, \phi_i) =$$
$$\frac{1}{\mu_i} e^{-\kappa_n d/\mu_i} \Gamma(\mu_i) A_1(\mu_i, \phi + \pi; \mu_i, \phi_i) \Gamma(\mu_i) e^{-\kappa_n d/\mu_i} + \frac{1}{\mu_i} e^{-\kappa_n d/\mu_i} \Gamma(\mu_i) A_2(\mu_i, \phi + \pi; \mu_i, \phi_i)$$
$$+ \frac{1}{\mu_i} A_3(\mu_i, \phi + \pi; \mu_i, \phi_i) \Gamma(\mu_i) e^{-\kappa_n d/\mu_i} + \frac{1}{\mu_i} e^{-\kappa_n d/\mu_i} A_4(\mu_i, \phi + \pi; \mu_i, \phi_i), \quad (3.12)$$

where the A_j terms are integrals of the extinction/phase matrices over the scatterer region and are defined as

$$A_1(\mu, \phi; \mu_i, \phi_i) = \int_{-d}^{0} e^{-\kappa_n (d+z')/\mu} P_n(-\mu, \phi, \mu_i, \phi_i) e^{-\kappa_n (d+z')/\mu_i} dz',$$

$$A_2(\mu, \phi; \mu_i, \phi_i) = \int_{-d}^{0} e^{-\kappa_n (d+z')/\mu_i} P_n(-\mu, \phi, -\mu_i, \phi_i) e^{-\kappa_n (z')/\mu_i} dz',$$

$$A_3(\mu, \phi; \mu_i, \phi_i) = \int_{-d}^{0} e^{-\kappa_n (z')/\mu_i} P_n(\mu, \phi, \mu_i, \phi_i) e^{-\kappa_n (d+z')/\mu_i} dz',$$

and

$$A_4(\mu, \phi; \mu_i, \phi_i) = \int_{-d}^{0} e^{-\kappa_n (z')/\mu} P_n(\mu, \phi, \mu_i, \phi_i) e^{-\kappa_n (d+z')/\mu_i} dz'. \quad (3.13)$$

Γ is the reflection matrix as described by (3.1), and simply accounts for specular reflection from the ground. The angles of (3.12) are explicitly chosen for the case of backscatter. The impulse caused by the specular reflection at $\theta_i = 0$ was ignored. The results are shown in Fig. 3.7 for two different frequencies. No cross polarization is observed which is a direct result of the symmetry of the spherical scatterers as well as the first order solution to the VRTE. As expected, the backscatter at 5GHz is higher than that at 2GHz as a result of the larger relative scatterer sizes causing a greater attenuation. In both cases the $VV-$ and $HH-$ backscatter coefficients diverge from each other off of nadir incidence. This is a direct result of the ground scattering and the Fresnel reflection coefficients. For a half-space of purely spherical scatterers, both polarizations would be identical. The convergence of the two polarizations in the case of 5GHz is a result of the attenuation of the medium. If we consider the problem in terms of individual path lengths, then these path lengths are a function of the incident angle. The total path distance for a specified incident angle is $p(\mu) = 2d/\mu$. Therefore, at grazing incidence, the longer path length will result in greater attenuation through the media, which in turn dominates any difference between the Fresnel reflection coefficients for this case.

Fig. 3.8 and Fig. 3.9 shows the Co- and Cross- Polarization signatures for a random layer

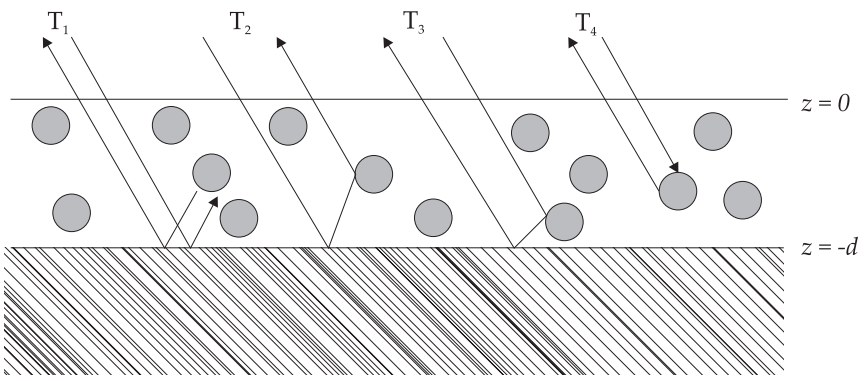

Figure 3.6: Scattering terms for the first-order solution to the single layer VRTE.

of dielectric discs and spheres, appropriate for simulating leaves, above a dielectric ground. The incident angle is 35°, with the same depth, dielectric constant, and radius used in the preceding examples. The height of the discs is 0.2 mm. In this case, the dielectric discs are uniformly distributed across all orientation angles, and the disk and sphere have the same radius and dielectric constant. These figures reveal that a dielectric disc uniformly distributed across all possible orientation angles can be modeled by an equivalent dielectric sphere. In other words, because the disc has an equal probability of being oriented at any possible position of (α, β, γ), the average scattering is approximately isotropic. Therefore, a dielectric sphere can be used in place of a uniformly distributed disc with little loss of accuracy. As the main topic of this paper is the development of a general remote sensing model, dielectric spheres will henceforth be used to model discs. As the phase and extinction matrices are much simpler for the case of spheres, this will aide in model complexity. Furthermore, in practice, these quantities can be accurately measured for different forest or volume types and as a result the actual model used in this thesis is of little importance.

From Fig. 3.8, we see that the strongest co-polarized returns are experienced for the linear polarizations. For the return is higher for HH- polarization, given by $\chi = 0°$, $\psi = \pm 45°$, then for VV- polarization $(0°, 0°)$ which is a result of the difference in Fresnel reflection coefficient. The co-polarized circular returns were negligible as expected. For the case of cross-polarized returns, Fig. 3.9, the circular polarization returns are the highest. This, too, is expected as the backscatter from a volume of spheres with a circularly polarized wave will be reversed in polarization. In other words, a right-handed circular wave will result in a left-handed circular wave being backscattered [Collin, 1985].

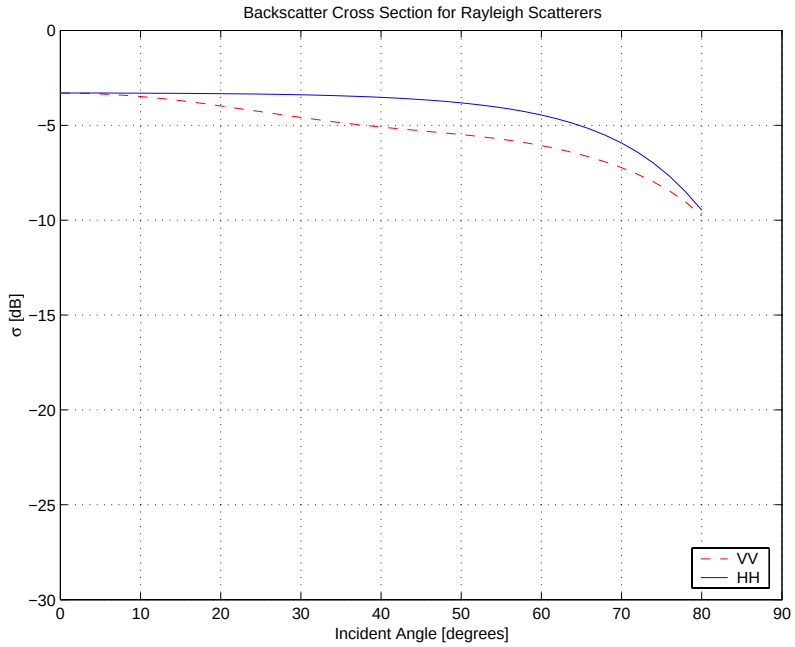

(a)

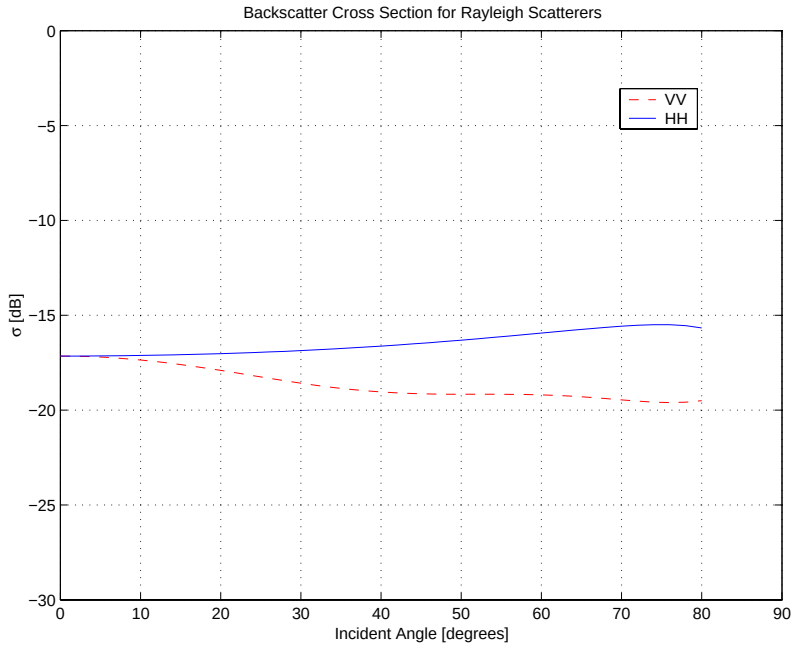

(b)

Figure 3.7: Backscatter at (a) 5GHz and (b) 2GHz from 1m layer of $a = 1cm$ spheres with $\epsilon_r = 5 + j$ and fractional volume of 0.4% above dielectric half-space with $\epsilon_r = 10 + j$.

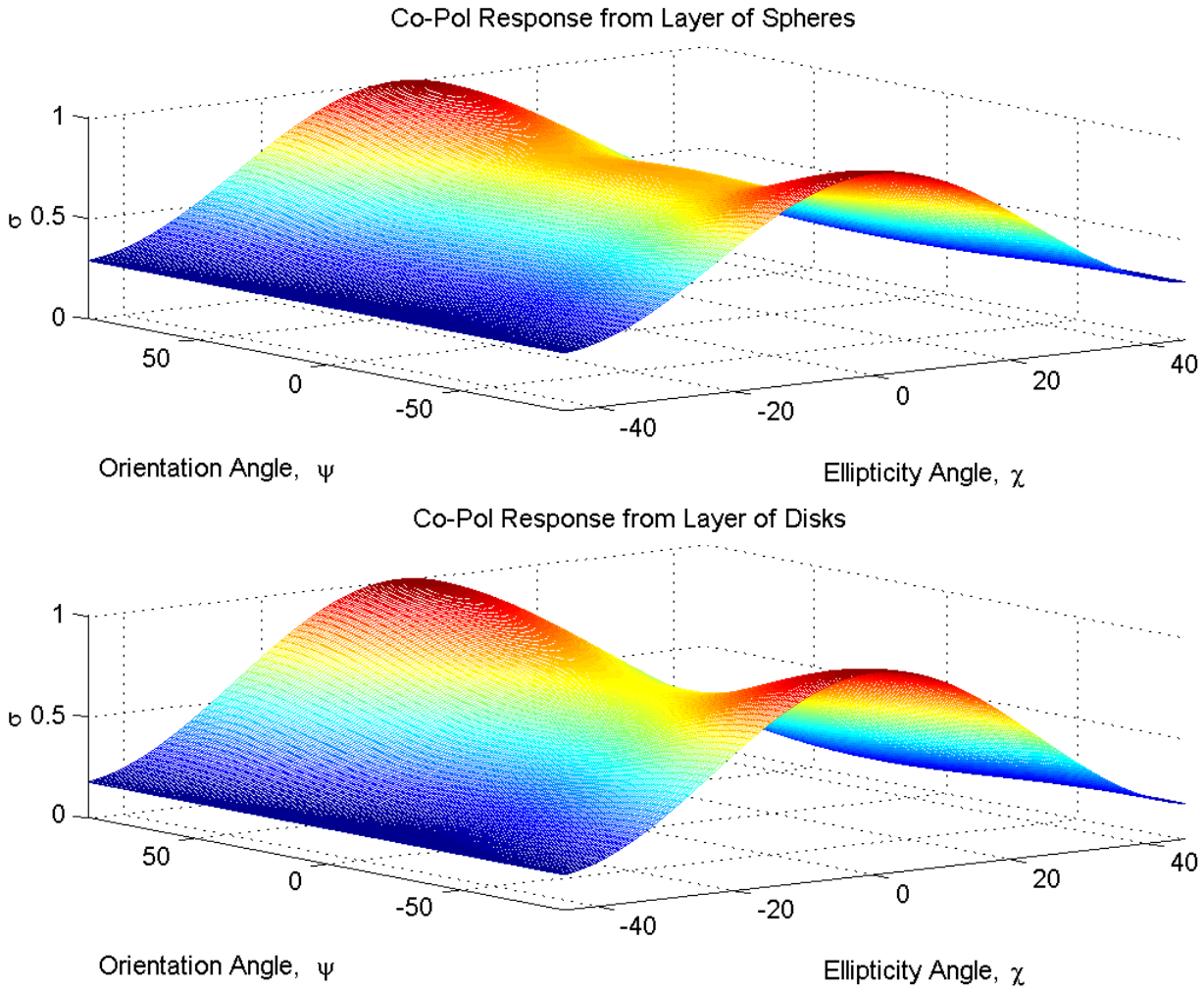

Figure 3.8: Co- Polarization Signatures for a layer of (top) spheres and (bottom) discs above a dielectric ground.

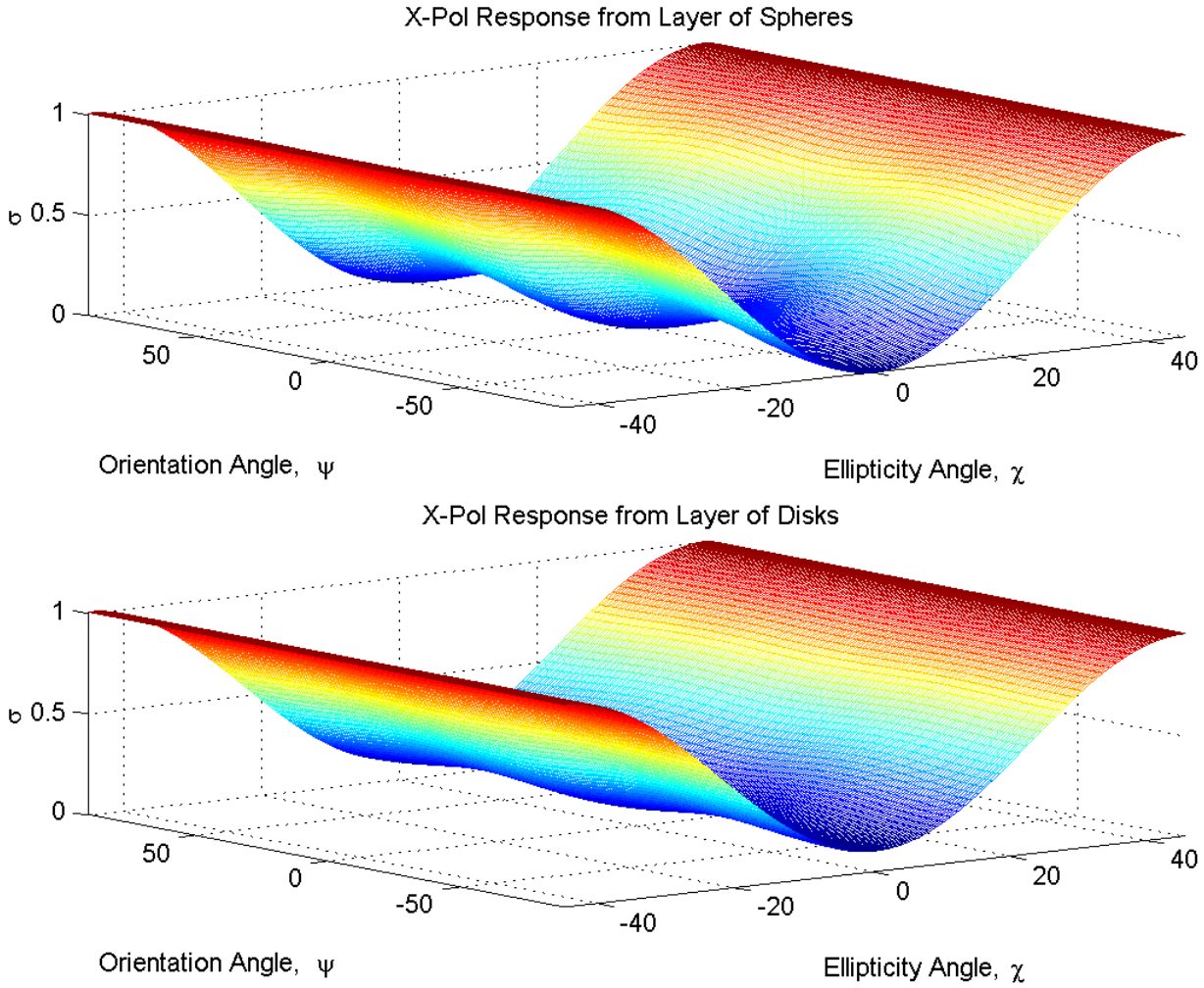

Figure 3.9: Cross Polarization signatures for a layer of (top) spheres and (bottom) discs above a dielectric ground.

Chapter 4

The Pulse Vector Radiative Transfer Equation

Until this point, all discussion has centered around the use of the time-harmonic vector radiative transfer equation to model the backscatter coefficient of foliage. This chapter will introduce the Pulse VRTE (PRVTE) which is simply a time-dependent form of the VRTE.

In applications such as remote sensing, the scattering of a random medium by an incident pulse is often desirable. In many radar applications, a pulse is used for detection and ranging, as well as effective extraction of target parameters; whether the target is the vegetation and terrain, or an underlying vehicle.

There exist several existing solutions to the Pulse VRTE. In [Ishimaru et al., 2001], and [Chang and Jin, 2002] Fourier transforms are employed to convert the VRTE back and forth between the time- and frequency- domains. The former relies on a discrete ordinates approach to solve the resulting intro-differential equation numerically while the latter relies on the iterative technique for the first order solution, similar to the technique outlined in §2.5. The discrete ordinate approach, while a common solution to numerically solving the VRTE, is computationally expensive as it requires the storage and solution of matrix equations. This method inherently overcomes some of the aforementioned density issues associated with the iterative solution, however, as discussed in the previous section the density and scattering behavior of most foliage canopies are low volume density, and small albedo; thereby making the iterative solution accurate in these applications. The latter model uses an iterative technique, however, it restricts itself to an incident Gaussian pulse and relies on an integral approximation to compute the integral, thereby binding the solution to a Gaussian pulse and obscuring physical insight into the actual scattering mechanisms. Furthermore, the approximation used to calculate the integral breaks down in the specular

and backward regions, thereby requiring a lengthy limit to be taken, further obscuring the underlying physics.

From the above synopsis, it is seen there exists a need for a *general*, simple expression for the Pulse VRTE, not restricted to incident waveforms or numerical methods. In this chapter, a path delay method will be described and employed by which the first-order, time-harmonic solution of §3.5 can be brought into the time domain. This will then be compared and contrasted with the solution obtained by Chang in [Chang and Jin, 2003]. Finally, from these expressions a first-order impulse response for a random volume will be found which allows for the fast and efficient calculation of direct random volume scattering .

4.1 Calculating Delays as a Function of Path Length

If the layered medium in Fig. 3.2 is excited by an incident intensity with an arbitrary waveform at $z = 0$, $t = 0$; the incident pulse will traverse through the medium until a scatterer is hit, at which point the intensity will be either reflected back toward the surface, or scattered into an arbitrary direction. The total time it takes for an intensity to be backscattered to the surface will be proportional to the path distance traversed by that intensity and related by the simple equation

$$\Delta t_j = \frac{\Delta d_j}{c_o} \tag{4.1}$$

where c_o is the speed of the intensity, which is be assumed to be the speed of light; and the j index corresponds to the terms in (3.6). Based on our model, c_o is the speed of light in free space. If the background media was not free space, the speed, c_o will be the speed of light through the background media.

Using the first-order solution, we are restricted to dealing with only four possible paths for a given intensity thereby requiring only four simple ray-traces, which can be further reduced to three by realizing two terms will result in the same over-all traversed distance. The geometries for the path distances are shown in Fig. 4.1. It is important to note that the ray paths are dependent on the variable of integration, z', which must thereby be incorporated into the total path length. The distances for each term in the backscatter case become

$$\begin{aligned}\Delta d_{gng}(z) &= 2\sum_{l=1}^{N}\frac{d_l}{\mu_i} + 2\sum_{l=n+1}^{N}\frac{d_l}{\mu_i} + 2\frac{|z_n| - |z'|}{\mu_i} \\ &= 4\frac{|Z_N|}{\mu_i} - 2\frac{|z'|}{\mu_i},\end{aligned} \tag{4.2}$$

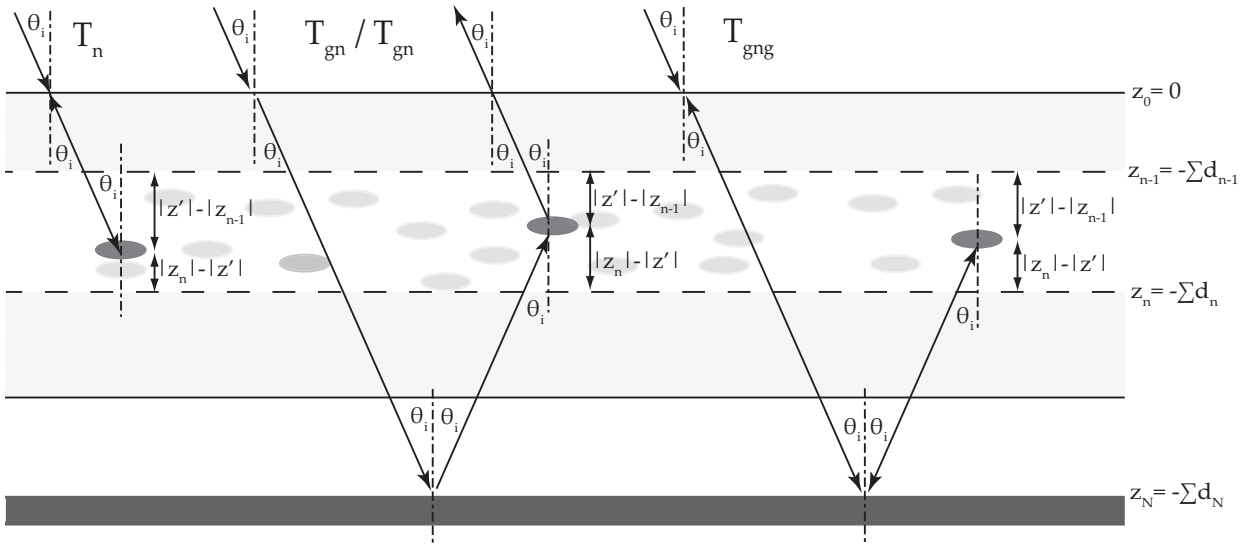

Figure 4.1: Ray-traces for first order multi-layered VRTE solution (direct ground term omitted).

$$\begin{aligned}\Delta d_{ng}(z) = \Delta d_{gn}(z) &= 2\sum_{l=1}^{N}\frac{d_l}{\mu_i} \\ &= 2\frac{|Z_N|}{\mu_i},\end{aligned} \tag{4.3}$$

and

$$\begin{aligned}\Delta d_n(z) &= 2\sum_{l=1}^{n-1}\frac{d_l}{\mu_i} + 2\frac{|z'| - |Z_{n-1}|}{\mu_i} \\ &= 2\frac{|z'|}{\mu_i}\end{aligned} \tag{4.4}$$

where

$$Z_n = \sum_{l=1}^{N} d_l$$

and z was forced to be positive to account for an integration from 0 to $-d$ in (3.6). For the case of Δd_{ng} and Δd_{gn} it is seen that the distance traveled in the backscatter case will always be independent of the variable of integration. This is a result of the specular ground, and

can be verified through examination of Fig. 4.1. The independence of the total path length from the variable of integration for these two terms provides a physical explanation for why the approximations in the equations of [Chang and Jin, 2002] and [Chang and Jin, 2003] do not hold in the specular and backscattered cases. Rather, instead of requiring a lengthy limit to be taken, these terms actually simplify in integral form; providing a key advantage in computations and physical understanding.

While the above ray-tracing procedure is performed for the backscattering case, it is straightforward to apply the same methodology to the bistatic case to obtain the correct path lengths and their corresponding delays.

4.2 The Transient Transformation Matrix

In §3.5 the Transformation Matrix for the case of a time-harmonic incident wave was given. It is therefore necessary to describe the incident and reflected intensities as a function of time. From the previous section, a collection of time delays for each term in the transformation matrix was found, thereby forcing the transformation matrix to be a function of the incident waveform.

First it is necessary to define the incident Stokes vector. Consider an incident intensity, $I_i(t)$ which can be described as the product of the time dependent scalar quantity (the waveform), $I_o(t)$, and the 4x1 Stokes vector, I'_o, as

$$I_i(t) = \begin{bmatrix} I_v \\ I_h \\ U \\ V \end{bmatrix} \cdot I_o(t) = I'_o I_o(t). \tag{4.5}$$

To describe the transformation matrix as a function of the incident waveform, the integrands of (3.6) must be multiplied by the waveform, $I_o(t)$, and delayed by the appropriate time delay, Δt. If the integrands of (3.6) are represented by $\Lambda_j(z')$, the general form of the time-delayed integrals will therefore be

$$A_j(t) = \int_{-z_n}^{-z_{n-1}} \Lambda_j(z') I_o(t - \Delta t'_j) dz' \tag{4.6}$$

where j can be either n, ng, gn, or gng. Physically, multiplying the original integrand by the delayed waveform serves to delay the contribution from the point z' by the time it would take a wave traveling at c_o to return to the surface represented by $z = 0$. Explicitly, the

integrands are

$$\Lambda_{gng}(z') = e^{-\kappa_n(z_n+z')/\mu} P_n(-\mu, \phi; \mu_i, \phi_i) e^{-\kappa_n(z'+z_n)/\mu_i} \tag{4.7a}$$

$$\Lambda_{ng}(z') = e^{-\kappa_n(z_n+z')/\mu} P_n(-\mu, \phi; -\mu_i, \phi_i) e^{+\kappa_n(z'+z_{n-1})/\mu_i} \tag{4.7b}$$

$$\Lambda_{gn}(z') = e^{+\kappa_n(z_{n-1}+z')/\mu} P_n(\mu, \phi; \mu_i, \phi_i) e^{-\kappa_n(z'+z_n)/\mu_i} \tag{4.7c}$$

$$\Lambda_{n}(z') = e^{+\kappa_n(z_{n-1}+z')/\mu} P_n(\mu, \phi; -\mu_i, \phi_i) e^{+\kappa_n(z'+z_{n-1})/\mu_i}. \tag{4.7d}$$

The transient transformation matrix is then represented by (3.5) with the integrals replaced with the expressions of (4.6), (4.7), and (4.2) - (4.4).

4.3 Example: Discs above a Dielectric Ground

To demonstrate the effectiveness of the ray-tracing approach to the transient transformation matrix, the matrix was computed for a 2.0 ns Gaussian pulse centered at 5.3 GHz incident upon a layer of random discs above a dielectric half-space. The scattering elements were spheres[1], with a radius of 2.5 cm, and a relative dielectric constant of 6.5+j2. The disks were located in a layer 3 m deep with a fractional volume of 0.55%, and the dielectric half-space had a relative permittivity of 15+j2. The pulse is of normalized Gaussian form

$$I_o(t) = e^{-(t-t_o)^2/2\sigma^2} \tag{4.8}$$

where σ is related to the half-power width of the pulse by $\sigma = T_{hp}/2\sqrt{2\ln 2}$, and t_o is an arbitrary delay.

For normal incidence, Fig. 4.3 - Fig. 4.4, the VV and HH backscatter is equal due to the spherical nature of the scatterers and the Fresnel reflection from the ground. In Fig. 4.3, the individual scattering paths are shown separately. First, the waveform component of the direct backscatter term appears, followed by the single scatter/reflection terms, and finally the double reflection terms. From this figure it is easily inferred that the double reflection term from the ground is generally very negligible. It is also easy to determine the effects that the path length and scattering have on the incident waveform. For the direct scatter term, T_n, the incident waveform is "smeared" and distorted. For the reflection/scatter terms, T_{ng}/T_{gn}, the backscatter waveform is identical to the incident waveform multiplied by a constant, as noted in the previous section. Finally, for the double bounce term, T_{ngn}, the backscatter is again "smeared" with a greatly attenuated magnitude. Fig. 4.4 demonstrates the total backscatter waveform with the individual returns incoherently added.

[1]Recall from previous sections that dielectric spheres are acceptable models for dielectric disks with an orientation described by a uniform probability density function.

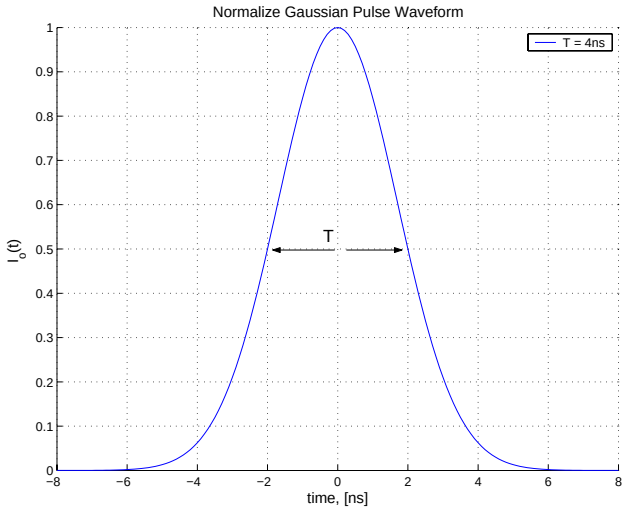

Figure 4.2: Normalized gaussian pulse waveform with a half-power width of T = 4 ns.

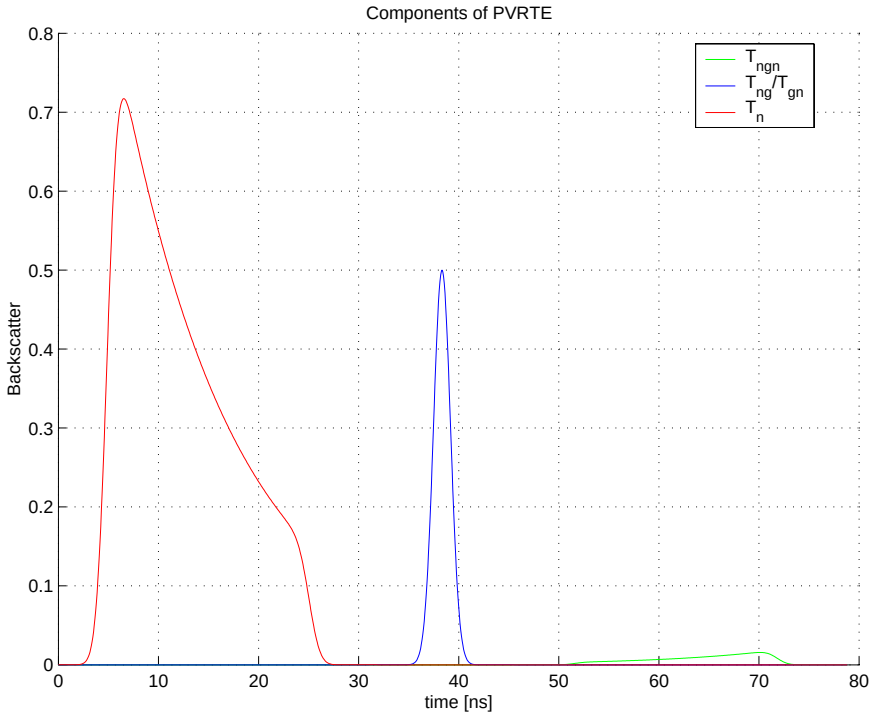

Figure 4.3: Backscatter waveform terms from Pulse VRTE simulation of a 3 m layer of spherical scatterers with a radius of 2.5 cm, and a relative dielectric constant of 6.5+j2, situated 2.0 m above a dielectric ground with $\epsilon_r = 15 + j2$.

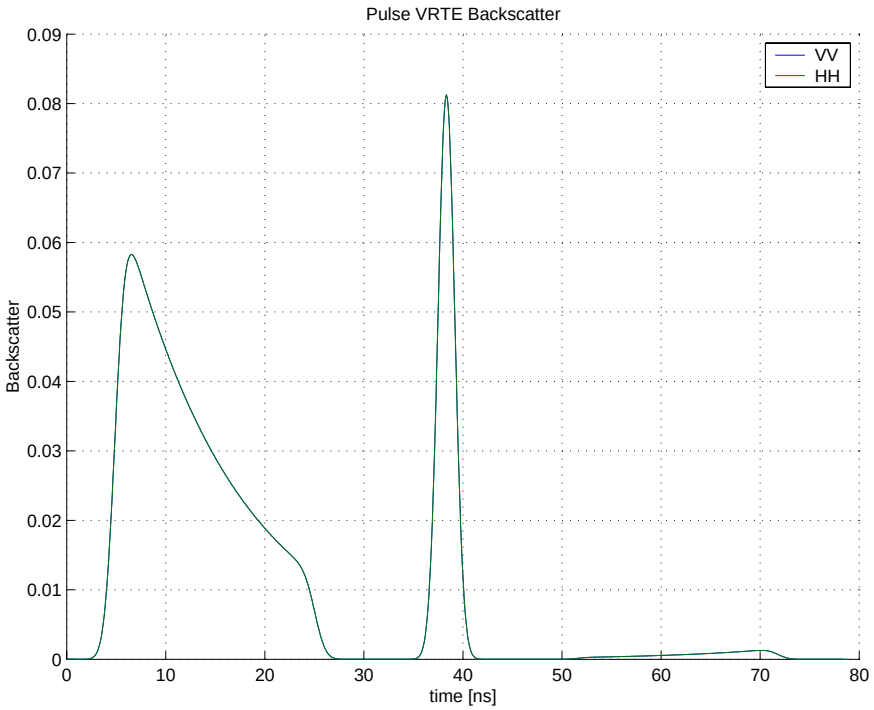

Figure 4.4: Backscatter waveform from Pulse VRTE simulation of a 3 m layer of spherical scatterers with a radius of 2.5 cm, and a relative dielectric constant of 6.5+j2, situated 2.0 m above a dielectric ground with $\epsilon_r = 15 + j2$.

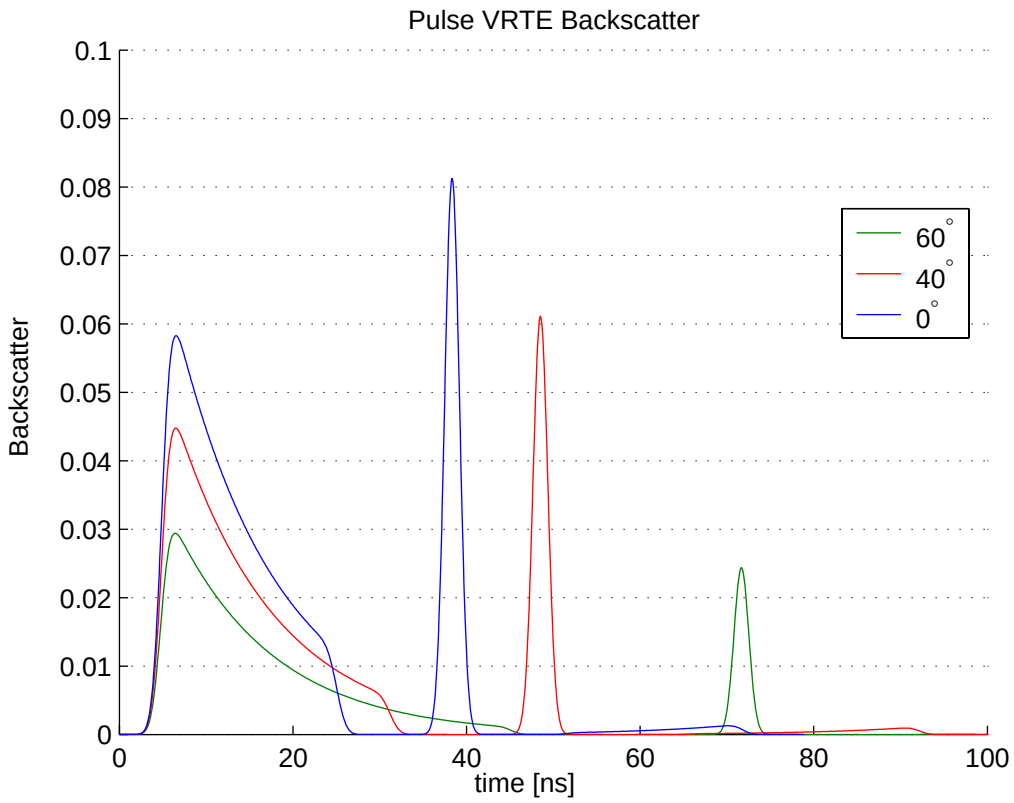

Figure 4.5: Horizontally polarized backscatter waveform from Pulse VRTE simulation of a 3 m layer of spherical scatterers with a radius of 2.5 cm, and a relative dielectric constant of 6.5+j2, situated 2.0 m above a dielectric ground with $\epsilon_r = 15 + j2$ for various incident angles.

If the angle of incidence, θ_i is varied, the path lengths of the respective terms will lengthen, thereby increasing the overall attenuation and broadening the backscatter returns. Graphically, this is seen in Fig. 4.5 for various incident angles.

4.4 The Volume Impulse Response

In the preceding sections, a technique was outlined by which, using several minor assumptions, time-dependence could be incorporated into the time-harmonic VRTE to model the backscatter waveforms of forest canopies and random volumes. While valid, the method of computing the waveform relies on performing a potentially burdensome numerical integration or approximation at each desired time increment. Alternatively, previous work on random volume and surface scattering by [Adams and Brown, 1998] and [Brown, 1977], have

indicated random scattering processes often lead to convolutional integrals. By defining the scattering process as the convolution of two terms, the computation can easily be performed using accurate and proven Fast Fourier Transforms (FFTs). FFTs introduce a greater, well understood degree of accuracy, and can be easily implemented in "real-time" using widely available digital signal processing boards. Furthermore, deconvolution algorithms exist which may in turn lead to an easy means to extract useful parameters from the returned waveform, assuming the scattering process can be expressed as a convolutional integral.

In order to derive the impulse response of a random volume from Radiative Transfer Theory, it is necessary to examine the integral represented by A_n given in (3.6) and rewritten below with the incorporated time dependence as,

$$A_n(z,t) = \int_{-z_n}^{-z_{n-1}} \Lambda_n I_o(t - \Delta t_n) dz' \tag{4.9}$$

$$\Lambda_n(z') = e^{+\kappa_n(z_{n-1}+z')/\mu} P_n(\mu,\phi;-\mu_i,\phi_i) e^{+\kappa_n(z'+z_{n-1})/\mu_i} \tag{4.10}$$

The above term is used in conjunctions with (3.4) to find the transformation matrix and therefore backscatter coefficient and polarization signature due to the direct scatter term. By defining a new variable in the time domain,

$$\tau = -\frac{2z'}{c_o\mu} = \Delta t_n$$

and performing a simple change of variables over the integral, Λ can be expressed purely as a function of time,

$$\Lambda_n(\tau) = e^{-\kappa_n(t-t_{n-1})c_o/2} P_n(\mu,\phi;-\mu,\phi) e^{-\kappa_n(t-t_{n-1})c_o/2} \tag{4.11}$$

where t_{n-1} is the time it takes to propagate to the top of the n^{th} layer and can be inferred from the definition of τ and Fig. 4.1. Substituting this expression back into the original integral yields an integration purely over time,

$$A_n(t) = \frac{c_o\mu}{2} \int_{t_n-1}^{t_n} \Lambda_n(\tau') I_o(t-\tau') d\tau' \tag{4.12}$$

$$\tag{4.13}$$

where $\Lambda(t)$ is given by (4.11). By recasting (4.11) as a piecewise function of

$$\Lambda_n(t) = \begin{cases} e^{-\kappa_n(t-t_{n-1})c_o/2} P_n(\mu,\phi;-\mu,\phi) e^{-\kappa_n(t-t_{n-1})c_o/2} & t_{n-1} \le t \le \frac{2d_n}{c_o\mu} + t_{n-1} \\ 0 & \text{else} \end{cases} \tag{4.14}$$

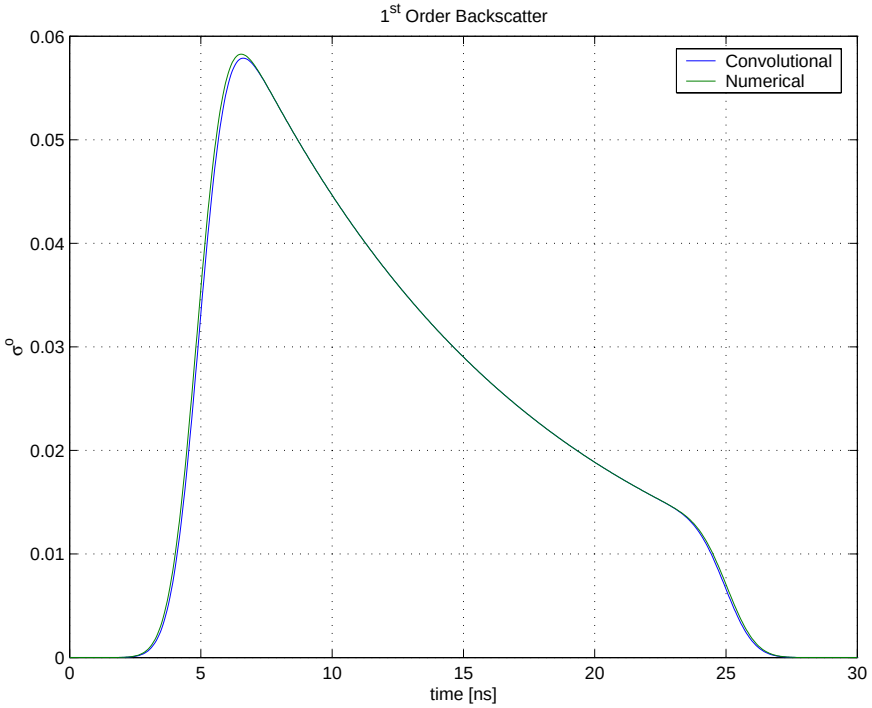

Figure 4.6: Comparison of direct backscatter coefficient for VV polarization for a single layer of dielectric spheres.

the limits of integration of (4.12) can be extended to $\pm\infty$, thereby resulting in the convolutional integral of

$$A_n(t) = \frac{c_o \mu}{2} \Lambda_n(t) \otimes I_o(t) \tag{4.15}$$

where $\otimes$ is the convolutional operator, Λ_n is defined by (4.14) and $I_o(t)$ is the original incident waveform. By recasting the radiative transfer integrand, Λ, as a function of time, the direct backscatter waveform can be directly computed through the use of FFTs as opposed to numerical approximations to the integral of (4.6). As no further assumptions beyond those originally associated with the ray-tracing approach have been introduced, (4.15) and (4.6) are identical. Fig. 4.6 compares the waveform computed using the numerical (midpoint integration) and convolutional (FFT) approaches. While the waveforms are nearly identical, using MATLAB signal processing routines for the FFTs yields a time savings factor of over 100 as compared to simple midpoint numerical integration schemes[2].

[2]A true rigorous comparison of computation is complicated by the numerous available algorithms for computing convolutions and numerical integrations.

Finally, the convolutional representation clearly indicates that the quantity Λ_n is the first order impulse response for a random volume. Fig. 4.7 shows a typical simulation for a 3 layer volume of spheres where the fractional volume of each level was varied. From the impulse response, Λ (top figure), the three distinct layers can be easily seen. The convolved backscatter waveform (bottom figure) shows the resulting backscatter from a Gaussian pulse.

4.5 Comments on the Accuracy and Limitations of the Transient Transformation Matrix

Comparing the resulting transient transformation matrix equation of the previous section with ones found in [Chang and Jin, 2002] reveals that they are identical, indicating that ray-tracing can be used to incorporate time dependence into iterative solutions of the VRTE. For the cases of volume scattering followed by specular reflection from the ground or its inverse term, ng or gn, the importance of the the path delay method can easily be seen: the constant delays of (4.3) indicate that this term is not dependent on the variable of integration, z', and can consequentially be removed from the integrals. Therefore,

$$\begin{aligned} A_{ng/gn} &= \int_{-d}^{0} \Lambda_{ng/gn}(z') I_o(t - \Delta t'_{ng/gn}) dz' \\ &= \int_{-d}^{0} \Lambda_{ng/gn}(z') I_o\left(t - \frac{\Delta d_{ng/gn}}{c_o}\right) dz' \\ \therefore A_{ng/gn} &= I_o\left(t - \frac{\Delta d_{ng/gn}}{c_o}\right) \int_{-d}^{0} \Lambda_{ng/gn}(z') dz', \end{aligned} \tag{4.16}$$

indicating that for terms involving a singular reflection from a specular ground, the returned waveform should be identical to that of the transmitted waveform multiplied by a scaling factor and delayed by (4.3). The independence of the integral from the incident waveform offers an explanation for why the integral approximations of [Chang and Jin, 2002] [Chang and Jin, 2003] break down in the backscatter direction: the approximations rely on a Gaussian waveform, resulting in a Gaussian integral; however, it is easily seen that in the backscatter direction, the integral is no longer Gaussian as the waveform becomes independent of the variable of integration.

As the ray-tracing approach used to obtain the transient transformation matrix is based on the first order solution to the VRTE, all the limits associated with these methods still apply. Additionally, by changing the source waveform from a time-harmonic form to a pulse, a finite frequency band is being introduced. Therefore, the underlying properties of the scatterers must be constant over the incident source's frequency spectrum. This is also true for any

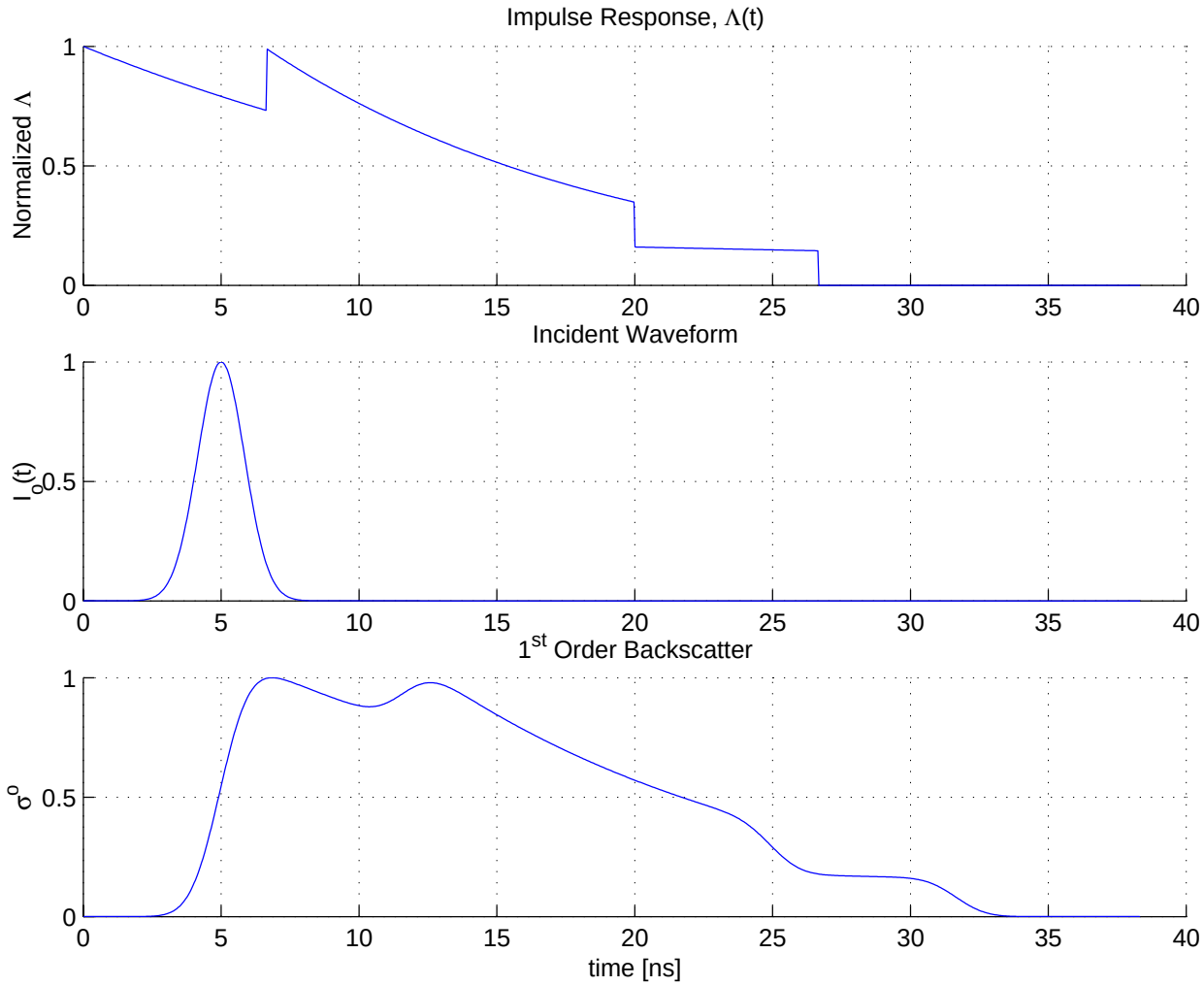

Figure 4.7: Impulse Response and backscatter waveform of a multi-layered canopy with the ground return omitted.

underlying dielectric ground. Simply stated, the scattering effects are frequency independent over the bandwidth of the incident waveform.

Chapter 5

The Impulse Response & Convolutional Models for Remote Sensing of Foliage

In remote sensing of natural phenomena, a large amount of information can be extracted from the returned waveform. Successful models have been developed for the ocean surface [Brown, 1977], as well as for ice and snow layers [Newkirk and Brown, 1996] [Adams and Brown, 1998]. While a waveform model was developed in the previous section for foliage, it fails to predict various effects the overall antenna system may have on the returned waveform; such as the beamwidth, altitude, and transmission loss to the foliage itself. Furthermore, successful models have been previously developed which account for all these factors and using convolutions, referred to herein as "convolutional models" [Adams and Brown, 1998] [Brown, 1977]. The advantage to the convolutional models is that the integrals normally associated with surface or volume scattering are now recast into a form readily computed using fast Fourier transforms (FFTs), facilitating in both the computation of the expected waveforms and extraction of useful parameters from returned waveforms. While many of these models are efficient and accurate, they deal only with scalar quantities. Recent advances in synthetic aperture (SAR) and other polarimetric radars have lead to an increased need for polarimetric radar equations and models. SAR technology has been used extensively in recent years to monitor foliage return, however, comprehensive, efficient, physics-based models capable of predicting the return are still scarce.

This chapter will focus on developing Volume Scatter Impulse Responses (VSIRs), which model the radar backscatter from penetrable, geophysical media. Unlike previous models, which also account for surface roughness effects, the developed model will only account for volume scattering effects. This is largely in part because the current surface scatter models

are already adequate. The current volume scattering models, conversly, are much more problem specific. This chapter will resolve this issue by developing a volume scatter model capable of simulating multi-layer foliage returns, but based on a broad Vector Radiative Transfer approach capable of modeling a much broader class of random volumes.

The general approach to deriving surface/volume impulse responses is as follows:

1. Use the Radar Equation to determine the backscattered power from an elemental surface or volume element, dS' or dV'. This term represents the incremental power contribution from an element in the surface/volume, dP_r.
2. Calculate the time delay associated with a round trip path from radar platform to the elemental area, $\Delta t'$. Multiply dP_r by the delayed impulse function $\delta(t - \Delta t)$.
3. Using the antenna pattern gain, sum over all illuminated surface/volume elements to find the total returned power.

This same approach will be applied to RT theory in order to develop a new convolutional model.

5.1 The Volume Scattering Impulse Response

The *volume scattering impulse response* (VSIR) for radar applications was developed in [Newkirk and Brown, 1996] to model the return from a penetrable volume. Fig. 5.1 shows the geometry of the VSIR. The radar is located at a height, $z = h$, above a penetrable volume. The surface of the volume is the xy plane. The radar illuminates an incremental volume element, dV, a radial distance r' from the radar, and described by azimuthal and elevation angles ϕ' and θ'. The incremental volume, dV' is always located below the surface $z = 0$. For this application, only the nadir pointing case will be considered, however, the expressions and coordinates for the off-nadir case can be found in [Newkirk and Brown, 1994].

The general equation for the impulse response is then given as [Newkirk and Brown, 1994] [Newkirk and Brown, 1996]

$$P_{IR} = \frac{\lambda^2}{(4\pi)^3} \int_V \frac{G^2(\psi,\omega) T_b^2(\theta)}{r'^4} \delta\left[t - 2\left(\frac{r_i}{c_o} + \frac{r' - r_i}{c_s}\right)\right] \sigma_V^o dV' \tag{5.1}$$

where

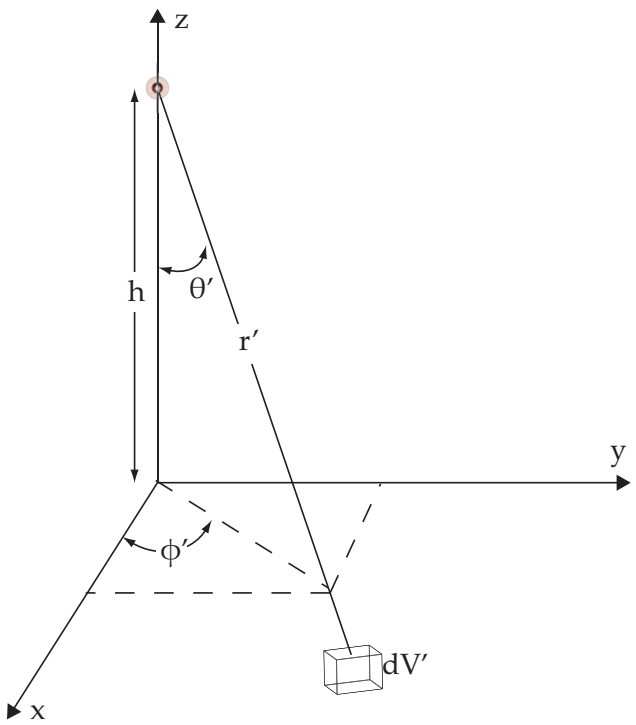

Figure 5.1: Geometry for the volume scattering impulse response (VSIR).

λ	Radar wavelength.
$T_b(\theta)$	Fresnel power transmission coefficient for background medium.
$G(\psi, \omega)$	Radar antenna gain pattern.
ψ	Angle relative to boresight axis.
ω	Rotation about boresight axis.
r'	Range to differential volume element.
r_i	Range to $z = 0$ surface interface, $r_i = h \cos\theta$.
c_o	Speed of light in free space.
c_s	Speed of light in dielectric background.
σ_V^o	Effective scattering cross factor.
dV'	Differential volume within medium ($r'^2 \sin\theta' dr' d\theta' d\phi'$).

and the impulse function, $\delta(\cdots)$ serves to delay the scattering contribution of the dV'-th volume element by the appropriate time factor. For the case of a layer of foliage with diffuse interfaces and no background dielectric, $c_s = c_o$ and the delay inside the impulse function becomes $-2r'/c_o$. For the case of a dielectric ground, $c_s \neq c_o$. While this method is very successful for many applications, the advancement of synthetic aperture radar (SAR) and other polarimetric radars has lead to a need for a polarimetric volume impulse response

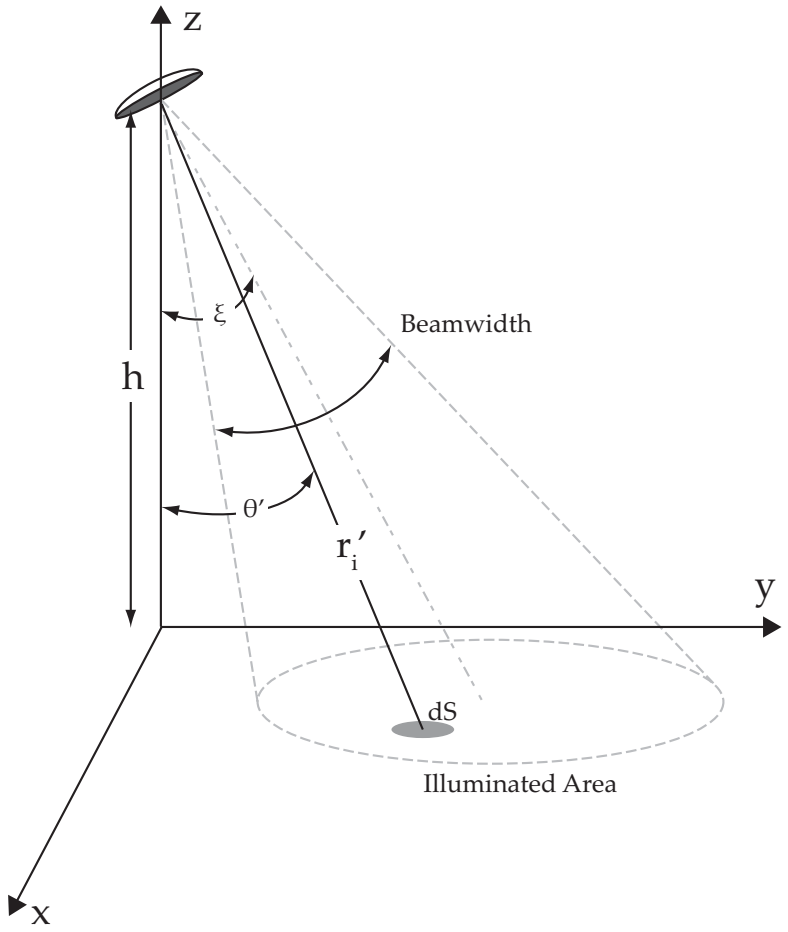

Figure 5.2: Radar platform located above a multi-layered folaige canopy.

equation of similar form.

5.2 The Stokes Vector Radar Equation

In §3.5, it was shown how a backscatter coefficient could be calculated using the transformation matrix for the case of linear polarizations. While this expression is suitable for use in the traditional Radar Equation, it is more desirable to obtain an expression for the Radar Equation in terms of the Stokes vector, thereby creating a more general expression for an arbitrary antenna polarization. To derive a suitable form for the radar equation using the Stokes vector, first consider an antenna system with a gain of $G(\theta, \phi)$ transmitting a polar-

ized wave with an amplitude of P_t. The antenna is located at a height, h, above the surface as shown in Fig. 5.2. The boresight is described by ξ, which is measured relative to nadir. The surface is assumed to be symetric in the azimuth direction causing the choice of ϕ to be arbitrary. The polarization described by the normalized[1] Stokes vector, $\mathbf{I}_{tn}$

$$\mathbf{I}_{tn} = \begin{bmatrix} \frac{1}{2}(1 + \cos 2\chi_t \cos 2\psi_t) \\ \frac{1}{2}(1 - \cos 2\chi_t \cos 2\psi_t) \\ \cos 2\chi_t \sin 2\psi_t \\ \sin 2\chi_t \end{bmatrix} \tag{5.2}$$

where ψ_t and χ_t are the orientation and ellipticity angles of the transmitted polarization. Using the transformation matrix, $\mathbf{T}$, of §3.5, the polarization signature of the random media at the $z = 0$ surface is given by (§3.6)

$$\mathcal{P}_s = \mathbf{h}^{\mathrm{T}} \mathbf{T} \mathbf{I}_{tn} \tag{5.3}$$

where T is the transpose operator and $\mathbf{h}$ is the complex effective antenna height, given as

$$\mathbf{h} = \begin{bmatrix} \frac{1}{2}(1 + \cos 2\chi_r \cos 2\psi_r) \\ \frac{1}{2}(1 - \cos 2\chi_r \cos 2\psi_r) \\ -\frac{1}{2} \cos 2\chi_r \sin 2\psi_r \\ \frac{1}{2} \sin 2\chi_r \end{bmatrix} \tag{5.4}$$

which accounts for polarization matching between the receiving antenna and the EM wave incident on the receiving antenna. From the polarization signature, the backscattering coefficient at the $z = 0$ surface can be found using [Tsang and Ding, 1991]

$$\sigma^o = 4\pi \cos\theta_i \mathcal{P}_s. \tag{5.5}$$

Substituting (5.5) into the general Radar Equation yields the incremental power resulting from the illumination of the surface dS'

$$\begin{aligned} dP_r &= P_t \frac{\lambda^2 G^2(\theta', \phi') \sigma^o}{(4\pi)^3 (r_i')^4} dS' \\ &= P_t \frac{\lambda^2}{(4\pi)^3} \frac{G^2(\theta', \phi')}{(r_i')^4} \left[4\pi \cos\theta' \mathbf{h}^{\mathrm{T}} \mathbf{T} \mathbf{I}_{tn} \right] dS' \end{aligned}$$

[1]Normalization is performed such that $I_v^{in} + I_h^{in} = 1$.

and summing over all illuminated areas yields

$$P_r = P_t \frac{\lambda^2}{(4\pi)^3} \int_S \frac{G^2(\theta',\phi') \left[4\pi \cos\theta' \mathbf{h}^{\mathrm{T}} \mathbf{T} \mathbf{I}_{tn}\right]}{(r_i')^4} dS'. \tag{5.6}$$

$$= P_t \frac{\lambda^2}{(4\pi)^3} \int_S \frac{G^2(\theta',\phi') \left[4\pi \cos\theta' \mathcal{P}_s\right]}{(r_i')^4} dS'. \tag{5.7}$$

Equation (5.6) is a general form for incoherent power scattered from the time-harmonic illumination of a surface and accounts for polarimetric scattering through the use of the transformation matrix, $\mathbf{T}$, and the Stokes vector and effective height, $\mathbf{I}_{tn}$ and $\mathbf{h}$. In formulating (5.6), no assumptions have yet been made about the scattering process other than those associated with the general radar equation. In fact, (5.6) can account for either the reflection from an illuminated surface or columnated volume beneath the illuminated surface, depending on how the scattering process is modeled in $\mathbf{T}$. In the case of surface scattering, the scattering from the incremental illuminated areas, dS', must be independent of the other incremental areas. Likewise for the case of volume scattering, an incremental columnated volume beneath dS' must scatter independently of the other incremental illuminated columns. In this way, the problem is essentially being decomposed into two regions: a freespace region and a random volume region. In the freespace region, where $z > 0$, the Radar Equation is used to account for the radio wave propagation. In the random volume region, $z < 0$, Radiative Transfer theory is ued to model the propagation and scattering proceses.

5.3 The Polarimetric VSIR

The previous section demonstrated how the radar equation could be related to the time-harmonic radiative transfer quantities used to model layered vegetation. Next, the time-dependent radiative transfer solution developed in §4.2 can be used to determine the returned power waveform for an arbitrary incident pulse, as shown in Fig. 5.3. Using the definition of the polarization signature, (5.3), the power waveform resulting from the n^{th} layer is given by

$$P_r^n(t) = \frac{\lambda^2}{(4\pi)^3} \int_S \int_{-z_n}^{-z_{n-1}} \frac{G^2(\theta',\phi')}{(r_i')^4} \left[4\pi \mathcal{P}_n'(z')\right] P_t \left(t - 2\frac{r_i'}{c_o'} - \frac{2|z'|}{\mu' c_o}\right) dz' dS' \tag{5.8}$$

where the quantity

$$\mathcal{P}_n'(z') = \mathbf{h}^{\mathrm{T}} \cdot \left[\prod_{m=1}^{n-1} e^{-\kappa_m d_m/\mu}\right] \Lambda_n(z') \left[\prod_{m=1}^{n-1} e^{-\kappa_m d_m/\mu}\right] \cdot \mathbf{I}_{tn} \tag{5.9}$$

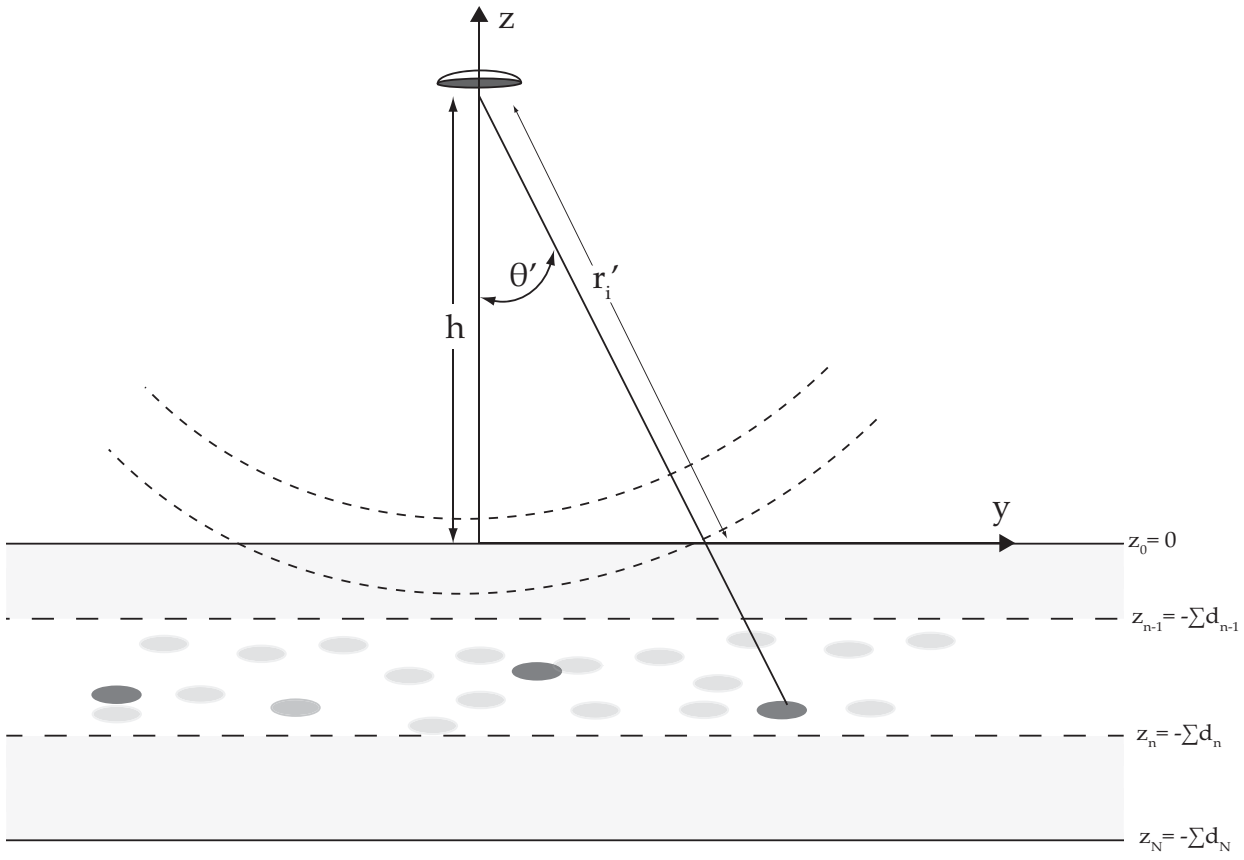

Figure 5.3: Radar platform located above a multi-layered folaige canopy.

is the component of the transient transformation matrix of §4.2 which accounts for the attenuation of the coherent wave to the n^{th} layer, followed by incoherent scattering at the z' point and attenuation of the scattered wave back to the $z = 0$ surface. The quantity $\Lambda(z)$ was defined in §4.2, equation (4.7). In the above formulation, the $I_o(t)$ notation used in the RT theory for the incident waveform has been replaced by $P_t(t)$ to denote the power waveform. Furthmore, the $\cos\theta'$ term present in the definition of the polarization signature is canceled out by the presence of a $1/\cos\theta'$ term in the definition of the transformation matrix. While this is potentially useful expression for predicting radar returns from polarimetric radar, it still requires a burdensome volume integration.

From §4.4, it was shown that a simple change of variables in the RT integrals transforms the the integration over z' to a convolution in the time domain. Applying this same technique to (5.8) and summing over all N layers yields

$$P_r = \frac{\lambda^2}{(4\pi)^3} \int_S P_t\left(t - 2\frac{r_i'}{c_o'}\right) \otimes \frac{G^2(\theta', \phi')}{(r_i')^4} \left[\sum_{n=1}^{N} 4\pi \cos\theta' \mathcal{P}_n'(t)\right] dS' \tag{5.10}$$

where

$$\mathcal{P}_n'(t') = \frac{c_o}{2}\mathbf{h}^{\mathrm{T}} \cdot \left[\prod_{m=1}^{n-1} e^{-\kappa_m d_m/\mu}\right] \Lambda_n(t') \left[\prod_{m=1}^{n-1} e^{-\kappa_m d_m/\mu}\right] \cdot \mathbf{I}_{tn} \tag{5.11}$$

and

$$\Lambda_n(t') = \begin{cases} e^{-\kappa_n(t-t_{n-1})c_o/2} P_n(\mu, \phi; -\mu, \phi) e^{-\kappa_n(t-t_{n-1})c_o/2} & t_{n-1} \le t \le \frac{2d_n}{c_o\mu} + t_{n-1} \\ 0 & \text{else.} \end{cases} \tag{5.12}$$

It should be noted that the $\Lambda(t')$ given above is identical to that derived in (4.14) and that $\mathcal{P}_n'(t')$ differs from $\mathcal{P}_n'(z')$ by a factor of $c_o/2$ and the choice of indepedent variable in Λ. Equation (5.11) and (5.10) represent the **P**olarimetric **V**olume **S**catter **I**mpulse **R**esponse (PVSIR) which accounts for the first-order scattering from a columnated random volume. Though it is similar in form to those found in [Adams and Brown, 1998] and [Newkirk and Brown, 1992], it is formulated using a slightly more rigorous radiative transfer approach and is therefore capable of modeling the response from an arbitrary polarization.

5.4 Modeling the Antenna Pattern

If the main beam of the antenna pattern can be approximated as an elliptical Gaussian beam, the expression for the gain is then given by [Newkirk and Brown, 1996]

$$G(\psi,\omega) = G_o e^{-\frac{2}{\gamma}(1+\beta\sin^2\omega)\sin^2\psi} \tag{5.13}$$

where

$$\gamma = \frac{2\sin^2(\sin\theta_s/2)}{\ln 2}$$
$$\beta = \frac{\gamma \ln 2}{2\sin^2(\theta_{xs}/2)} - 1$$

and θ_s and θ_{xs} are the 3-dB beamwidths of the E- and H- planes, respectively, of the corresponding receiving/transmitting antenna pattern and

$$\sin^2\omega = \frac{\tan^2\theta'\sin^2\phi'}{\tan^2\xi - 2\tan\xi\tan\theta'\cos\phi' + \tan^2\theta'}$$
$$\sin^2\psi = 1 - \cos^2\xi\cos^2\theta'\left[1+\tan\xi\tan\theta'\cos\phi'\right]^2.$$

If the pattern is symmetric, $\theta_s = \theta_{xs}$ and $\beta = 0$. While (5.13) is indeed useful for modeling purposes, any model can be used in the derived PVSIR. A typical pattern modeled from (5.13) is shown in Fig. 5.4.

5.5 Radar Returns using the PVSIR

The following simulations demonstrate typical backscatter waveforms resulting from the PVSIR simulations outlined in the previous sections. In all cases, the antenna was modeled as a nadir directed radar with $\theta_s = \theta_{xs}$, at a height of 10km or approximately 33 000 ft. Nadir directed radars offer the best foliage penetration, and are commonly used for radar altimeters. Nevertheless, the PVSIR is capable of modeling an arbitrary directed boresight. The foliage was modeled as a multi-layered volume of dielectric spheres with a radius, a, of 2.5 cm, and relative dielectric constant $\epsilon_{rs} = 6.5 + j2$. The integration over the angles θ' and ϕ' was carried out from 0 to $2\theta_s$[2] and 0 to 2π respectively using numerical integration. The incident pulse was Gaussian with a width of 1ns and offset of 5ns. All figures in this section are plotted versus an offset time, $t - 2h/c$, so that a time of zero corresponds to the earliest

[2]A complete integration over θ' is unnecessary as the antenna pattern is narrowly centered about nadir.

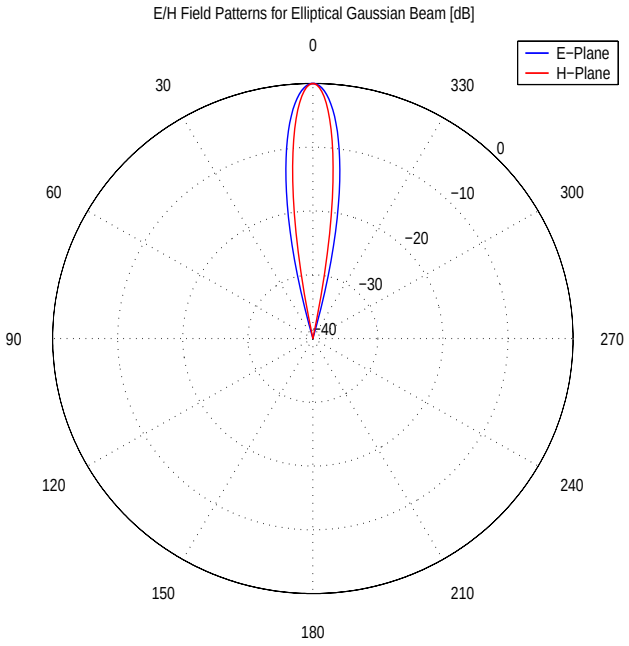

Figure 5.4: Elliptical gaussian beam pattern approximated by equation (5.13).

possible return expected from the random volume. Horizontal - Horizontal polarization is used, though based on the formulation, any arbitrary polarization can be simulated.

In Fig. 5.5, a single 2 m layer of foliage with a fractional density of 0.3% was simulated with various radar beamwidths. As the beamwidth is expanded, the backscatter waveform is broadened, or "smeared". This is the direct result of a larger illuminated area resulting in longer path delays down to the foliage interface. At $\theta = 0°$, the distance to the interface, r_i, is equal to the altitude, h, or 10 km. When $\theta \neq 0°$, as is the case with a finite beamwidth, the difference in path lengths between the nadir path and a path at an arbitrary angle, θ, is equal to $\Delta r_i = h(\sec\theta - 1)$. The extended path length correlates to a longer round trip propagation time from the radar to the foliage, which in turn leads to the dispersion of the returned power as the beamwidth is increased. Fig. 5.6 demonstrates the effects that the beamwidth dispersion has on discerning the individual layers of a foliage canopy. For this simulation, a 3 layer model was used with layer depths of 1m, 2m, and 1m, which correspond to fractional densities of 0.2%, 0.5% and 0.1%, respectively. As the beamwidth is increased, not only is the overall waveform broadened, but the distinct layers become indistinguishable due to the dispersion.

Fig. 5.7 demonstrates the similar effect using various pulse widths. All parameters are identical to those used in the previous simulation with the exception of the pulse width which

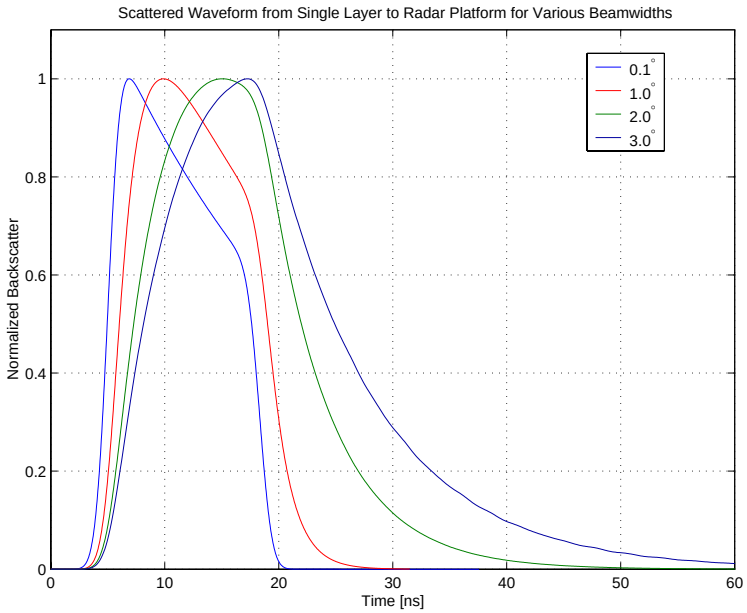

Figure 5.5: Radar return from 2 m layer of dielectric spheres with $f_v = 0.3\%$ illuminated by a nadir directed radar at an altitude of 10 km ($\approx$ 33000 ft).

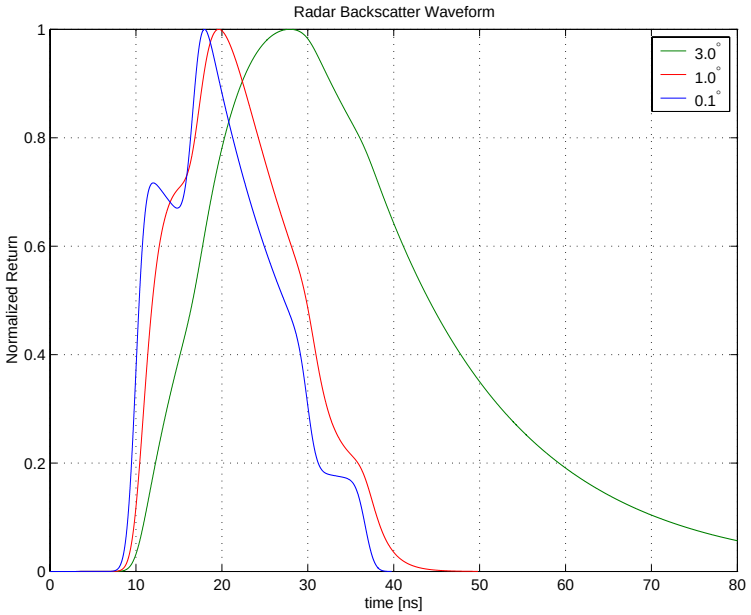

Figure 5.6: Radar return from 3 layers of dielectric spheres with various fractional volumes, and illuminated by a nadir directed radar at an altitude of 10km ($\approx$ 33000 ft).

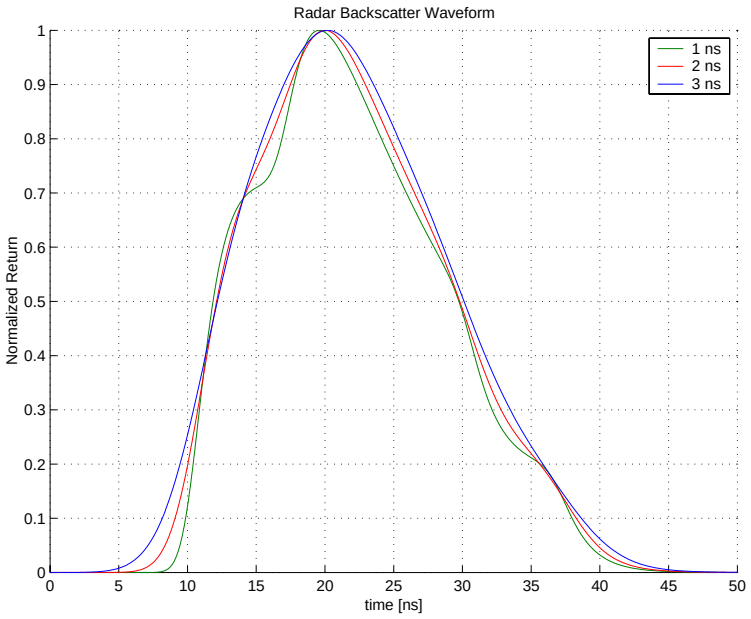

Figure 5.7: Radar return from 3 layers of dielectric spheres with various fractional volumes, and illuminated by a nadir directed radar with a 1° beamwidth at an altitude of 10 km ($\approx$ 33000 ft).

was varied and the pulse delay which was extended to 10 ns. As the pulse is broadened, the layers again become indistinguishable due to the decrease in the radar range resolution.

5.6 Development of a Convolutional Model

If assumptions can be accurately made about the scattering media or the antenna performance, the PVSIR can be further reduced in complexity. The first assumption that can be made, which is itself inherent in the VRTE formulation used to obtain (5.10), is that the media is described by uniform statistics in the azimuth direction. This, in turn, results in $\mathcal{P}'_n(t)$ being independent of ϕ. In the case of scalar VSIR, it was seen that the scattering coefficient could, in most cases, be completely removed from the integral leaving only an exponential attenuation factor inside the integral. Unfortunately, due to the introduction of polarization through Stokes vectors and matrices, the backscatter coefficient term, which is essentially Λ, cannot be directly moved from between the exponential terms due to the non-commutative nature of matrix multiplications.

Another assumption which can be made is in the case of a narrow-beam antenna. While such a system is not always used in remote sensing of vegetation, it is highly useful in radar altimeters as well as in radar systems used for target detection and classification. If

the narrow-beam assumption can be made, then $\mu' \approx \cos\xi$ in (5.12) and the time range over which a given layer "turns on" is approximately independent of μ. While the time range of Λ becomes independent of μ, the actual value of Λ may not be. Recalling that the phase matrix, P, is dependent on μ and the statistical orientation of the particles it is meant to simulate, it is possible, albeit unlikely, that Λ may still exhibit a dependence on μ. For remote sensing of foliage and natural geophysical media, it is anticipated that with the exception of regions where large specular scattering occurs, as discussed in (§3.3), over the small area illuminated by a narrow beam antenna the Phase matrix and therefore the polarization signature is approximately independent of μ.

Finally, the height of the radar above the foliage, h, should be much larger than the total depth of the foliage, d. This further ensures that the temporal variation of Λ caused by different incident angles is small compared to the time difference resulting from the propagation from the antenna to the volume interface. For a nadir directed antenna above a volume with a depth of d, the shortest time a ray can travel through the volume and back to the surface is proportional to $2(d+H)$. If the antenna has a finite beamwidth, it can be assumed that the longest time is proportional to a ray traveling at an angle equal to the beamwidth, resulting in a time of $2(d+H)/\cos\theta_{BW}$. The difference in these path lengths is what leads to the pulse distortion seen in Fig. 5.5 and Fig. 5.6. However, if $d << h$, the variation of d for the various incident angles is negligible and the difference between $2h$ and $2h/\cos\theta_{BW}$ is the dominant dispersion mechanism.

Applying the aforementioned assumptions to the PVSIR, the scattering process can be removed from the integration over ϕ to yield

$$P_r = \frac{\lambda^2}{(4\pi)^3}\int_\theta P_t\left(t - 2\frac{r_i'}{c_o'}\right) \otimes F(r_i')\left[\sum_{n=1}^{N} 4\pi\cos\theta'\mathcal{P}_n'(t)\right]d\theta' \tag{5.14}$$

where

$$F(r_i') = \frac{\sin\theta'}{(r_i')^2}\int_{2\pi} G^2(\theta',\phi')d\phi'.$$

Following [Brown, 1990]; using the property

$$\int_{-\infty}^{\infty} f(t')\delta(t'-t_o)dt' = f(t_o),$$

and assuming the scattering process, $\mathcal{P}$, is independent of incident angle over the illuminated

region, equation (5.14) can be recast as

$$P_r \approx \frac{\lambda^2}{(4\pi)^3}\left[\sum_{n=1}^{N} 4\pi\cos\theta_i \mathcal{P}'_n(t)\right] \otimes \int_{t'}\int_{\theta} P_t\left(t-t'\right)\delta\left(t'-\frac{2r'_i}{c_o}\right)F(r'_i)d\theta' dt'.$$

If two new quantities are defined as

$$\begin{aligned} P_{FS}(t) &= \frac{\lambda^2}{(4\pi)^3}\int_{\theta}\delta\left(t'-\frac{2r'_i}{c_o}\right)F(r'_i)d\theta' \\ &= \frac{\lambda^2}{(4\pi)^3}\int_{S}\delta\left(t'-\frac{2r'_i}{c_o}\right)\frac{G^2(\theta',\phi')}{(r'_i)^4}dS', \end{aligned} \tag{5.15}$$

and

$$P_{VI}(t) = \sum_{n=1}^{N} 4\pi\cos\theta_i \mathcal{P}'_n(t) \tag{5.16}$$

the returned waveform can be written as a double convolution,

$$P_r(t) = P_t(t) \otimes P_{FS}(t) \otimes P_{VI}(t). \tag{5.17}$$

Equation (5.17) reveals that the returned power waveform, $P_r(t)$, can be written in terms of the flat surface impulse response, $P_{FS}(t)$, and a volume scattering impulse response, $P_{VI}(t)$. Physically, the incident waveform is first distorted by the difference in pathlengths, r_i, due to the antenna beamwidth as well as the scattering processes within the random volume.

The flat surface impulse response (FSIR) defined in (5.15) is identical to those found in previous literature with the exception that it there is no dependence on a backscatter coefficient.This is a direct result of the diffuse boundaries associated with the current model. In this model, the FSIR is used to account for the time delay from the antenna to a diffuse interface; whereas previous models used the FSIR to account for the time delay and backscatter from a surface. Previously cited papers by Brown and Newkirk describe useful approximations for the FSIR which can also be used in the PVSIR model. For example, for a nadir directed radar with an elliptical Gaussian pattern described by (5.13), equation (5.15) can be written as

$$P_{FS}(t) \approx \frac{G_o^2(0^\circ)\lambda^2 c}{4(4\pi)^2 h^3} e^{-\frac{4\epsilon^2}{\gamma}\left(1+\frac{\beta}{2}\right)} I_o\left[\frac{2\beta\epsilon^2}{\gamma}\right] \tag{5.18}$$

where β/γ were defined previously, $\varepsilon^2 = ct/h$ and I_o is the modified Bessel function. Following previous standards, $t = 0$ corresponds to the time it takes to traverse a path distance of

$2h^3$.

5.7 Radar Returns using a Convolutional Model

The scattering process described by (5.17) was simulated using the multi-layered canopy described in the §5.5 for various antenna beamwidths. The approximation to the FSIR given by (5.18) was used to model the antenna beamwidth. The results are shown in Figures 5.8 - 5.10. From these figures, the effect that the beamwidth has on the FSIR, and subsequent returned power, is clearly seen . When the beamwidth is small, as shown in Fig. 5.8, the flat surface impulse response appears as a delta function about $t = 0$. As the beamdwidth is widened, the FSIR widens. The exponential decay of the FSIR is the result of the elliptical antenna gain pattern. Regardless of beamwidth, the volume impulse response, P_{VI}, is constant. Therefore, assuming a relatively heigh platform height, h, and narrow beamwidth, we can easily see that the dispersion experienced in the returned waveform is a direct result of the FSIR.

A comparison of the PVSIR computed using numerical integration and the convolutional approximation was also performed and shown in Fig. 5.11 - Fig. 5.13. From these figures, we see that both models are approximately equal. In the corresponding figures, the "exact" descriptor refers to a direct numerical integration of (5.10), where no assumption regarding a narrrow beam or platform height was made. The numerical integrations were performed by discritizing θ' and ϕ' to yield 4900 cells. Using built in convolution and FFT functions in Matlab, the convolutional implementation yielded a time savings factor of ≈ 5000 over a simple numerical integration approach. However, due to the numerous convolution and FFT algorithms and numerical integration techniques available, a more indepth speed comparison was not performed. Regardless, it is generally accepted that a convolution via FFTs will offer considerable time-savings over straight numerical integrations. Furthermore, as the beamwidth is broadened, more cells are needed for the numerical integration procedure to account for the larger illuminated area. This is evident in Fig. 5.13 where a small oscillation in the returned waveform of the "exact" model indicate a smaller cell size is needed to model the illuminated surface. The convolutional model has no such dependence on illuminated area and therefore is much quicker and more versatile.

[3]One roundtrip from the radar to the nearest point on the interface.

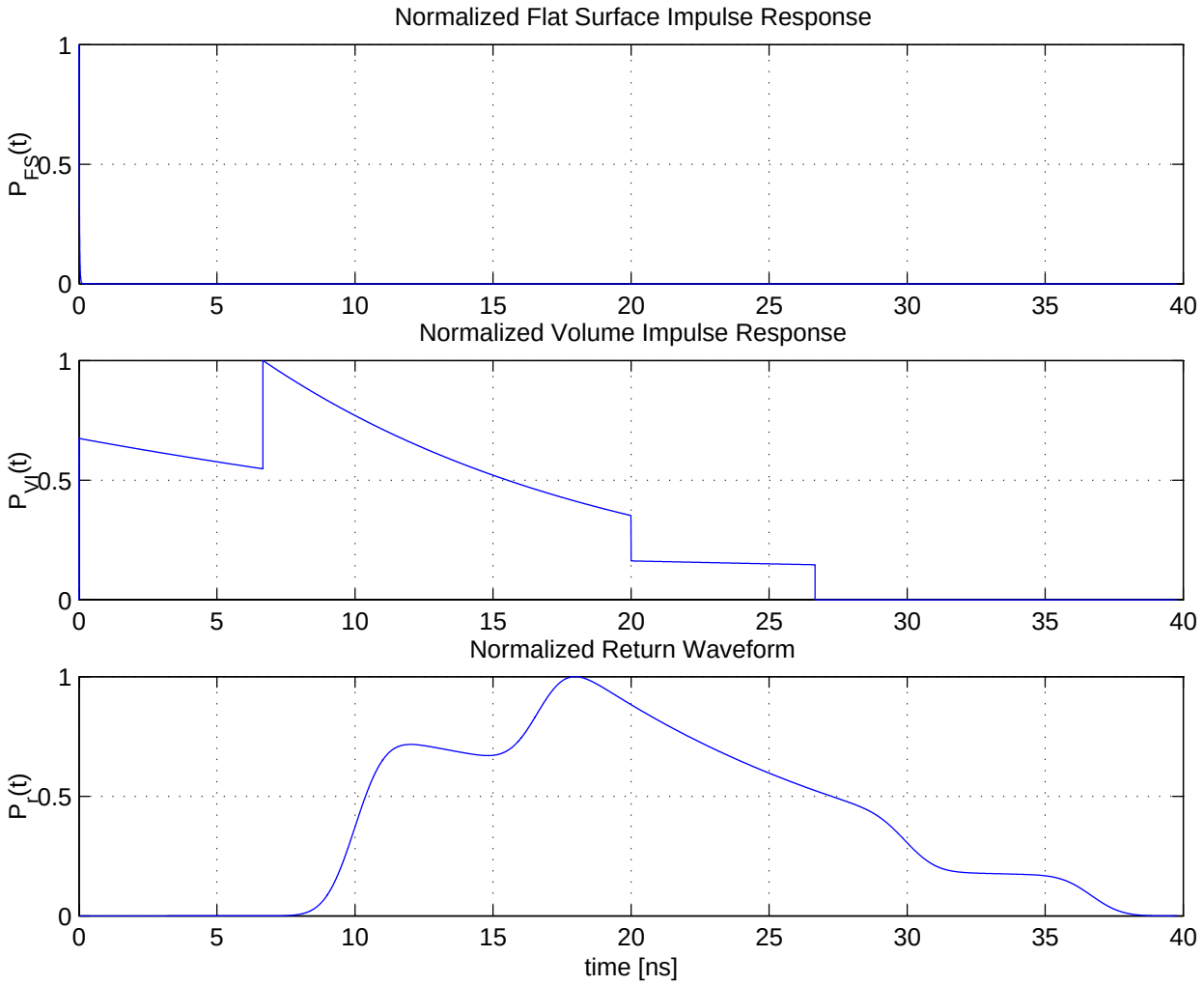

Figure 5.8: Impulse Responses for a random layered volume observed from a height of 10 km with a beamwidth of 0.1°.

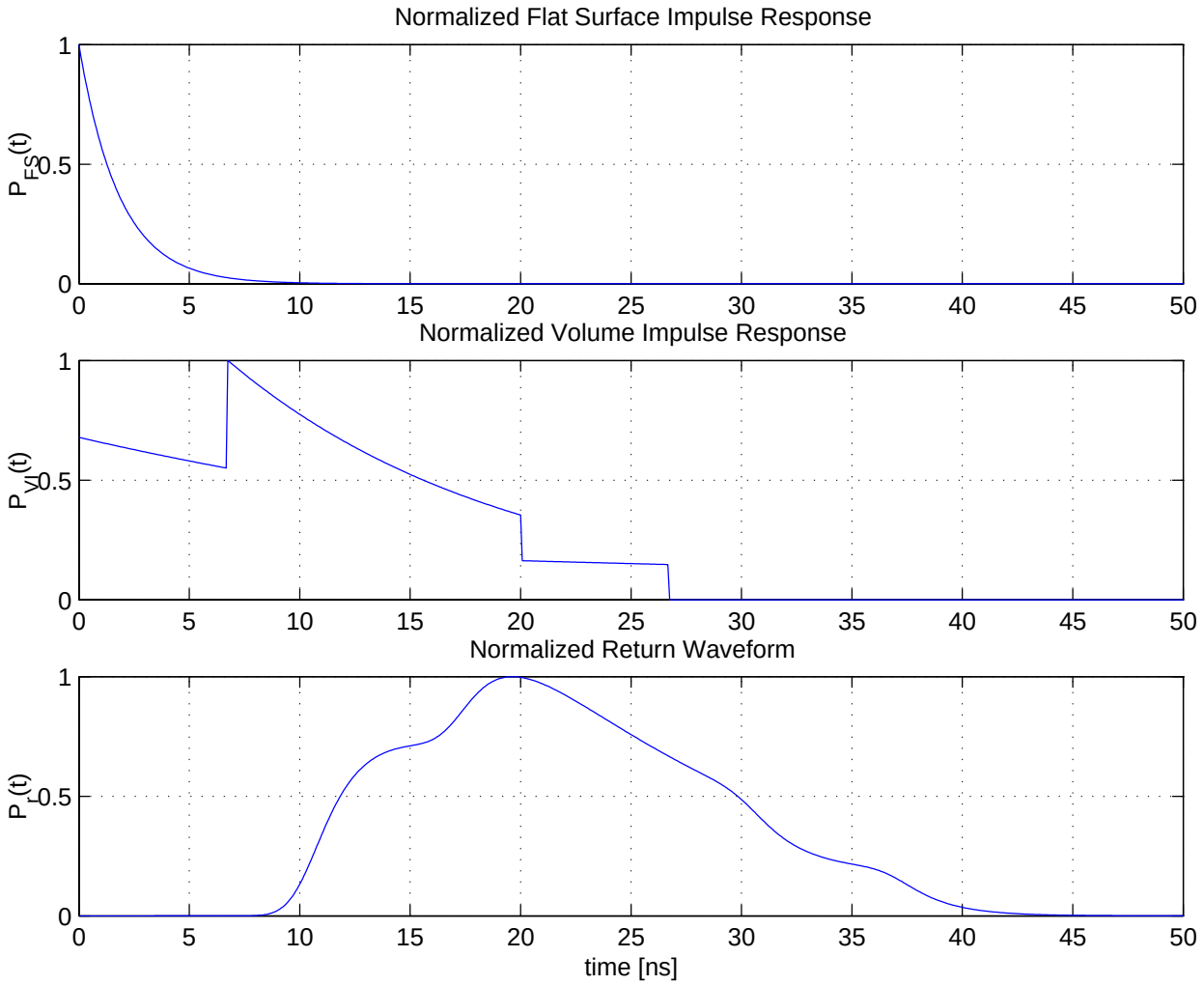

Figure 5.9: Impulse Responses for a random layered volume observed from a height of 10 km with a beamwidth of 1°.

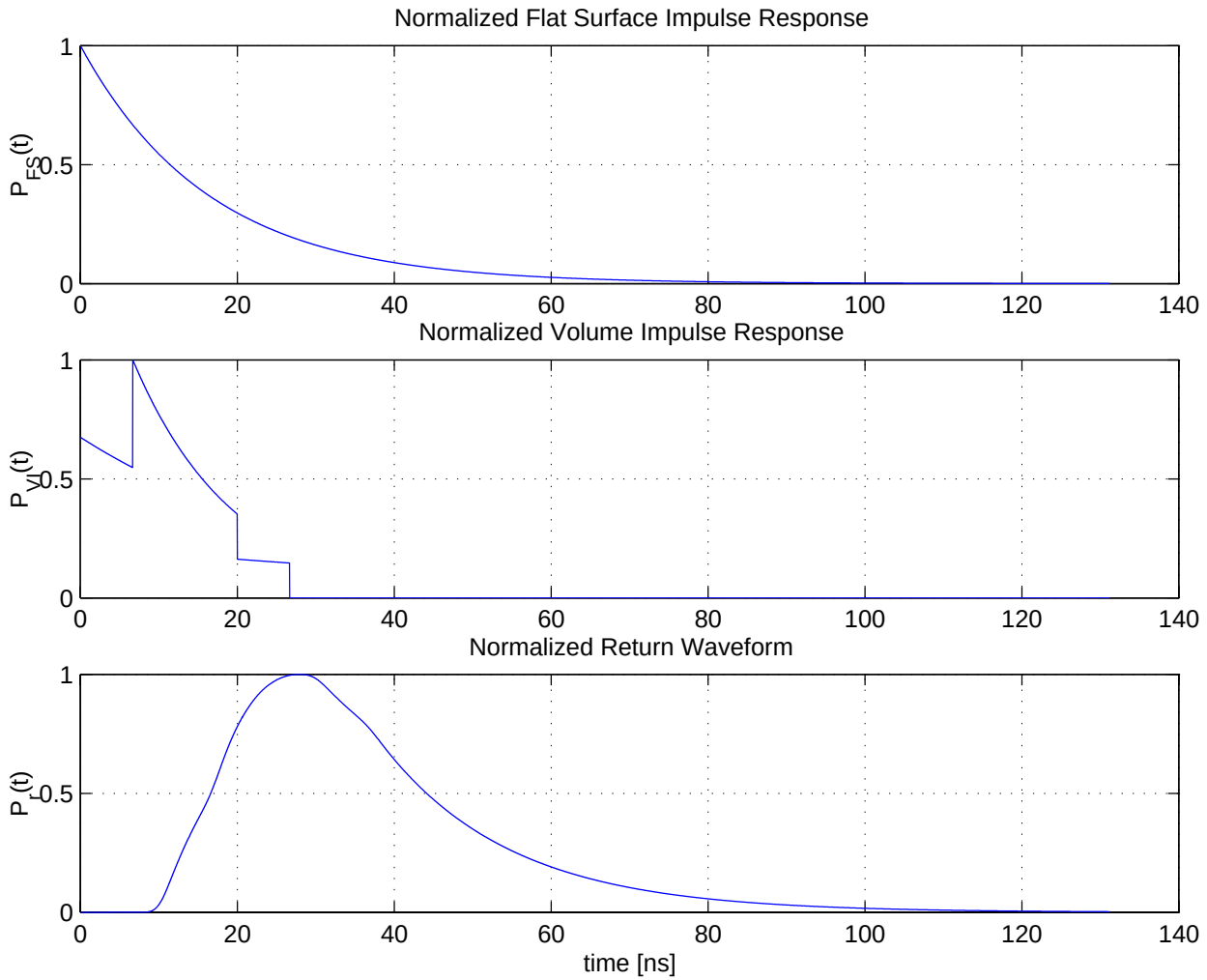

Figure 5.10: Impulse Responses for a random layered volume observed from a height of 10 km with a beamwidth of 3°.

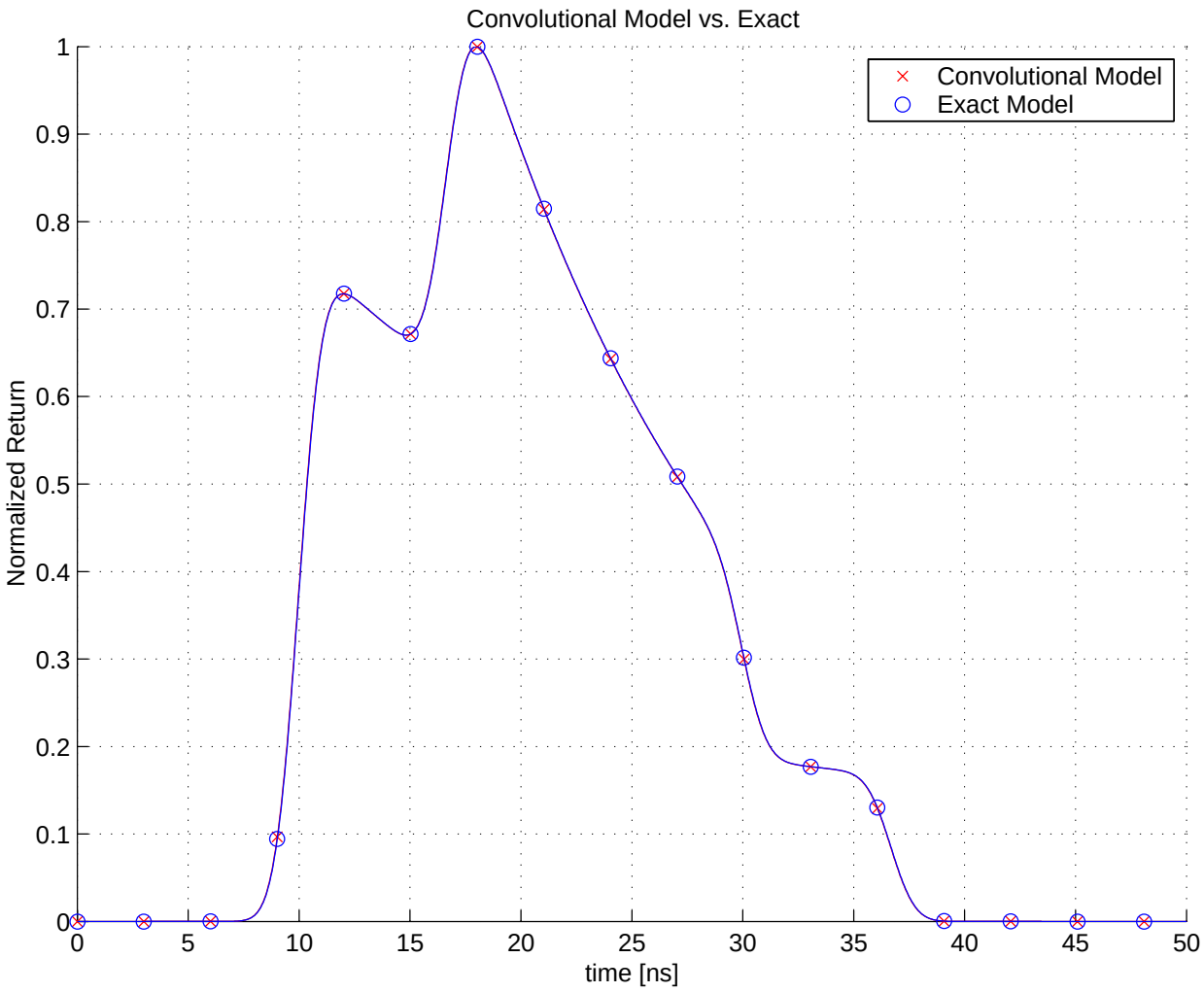

Figure 5.11: Comparison of convolutional model and exact model for a beamwidth of 0.1°.

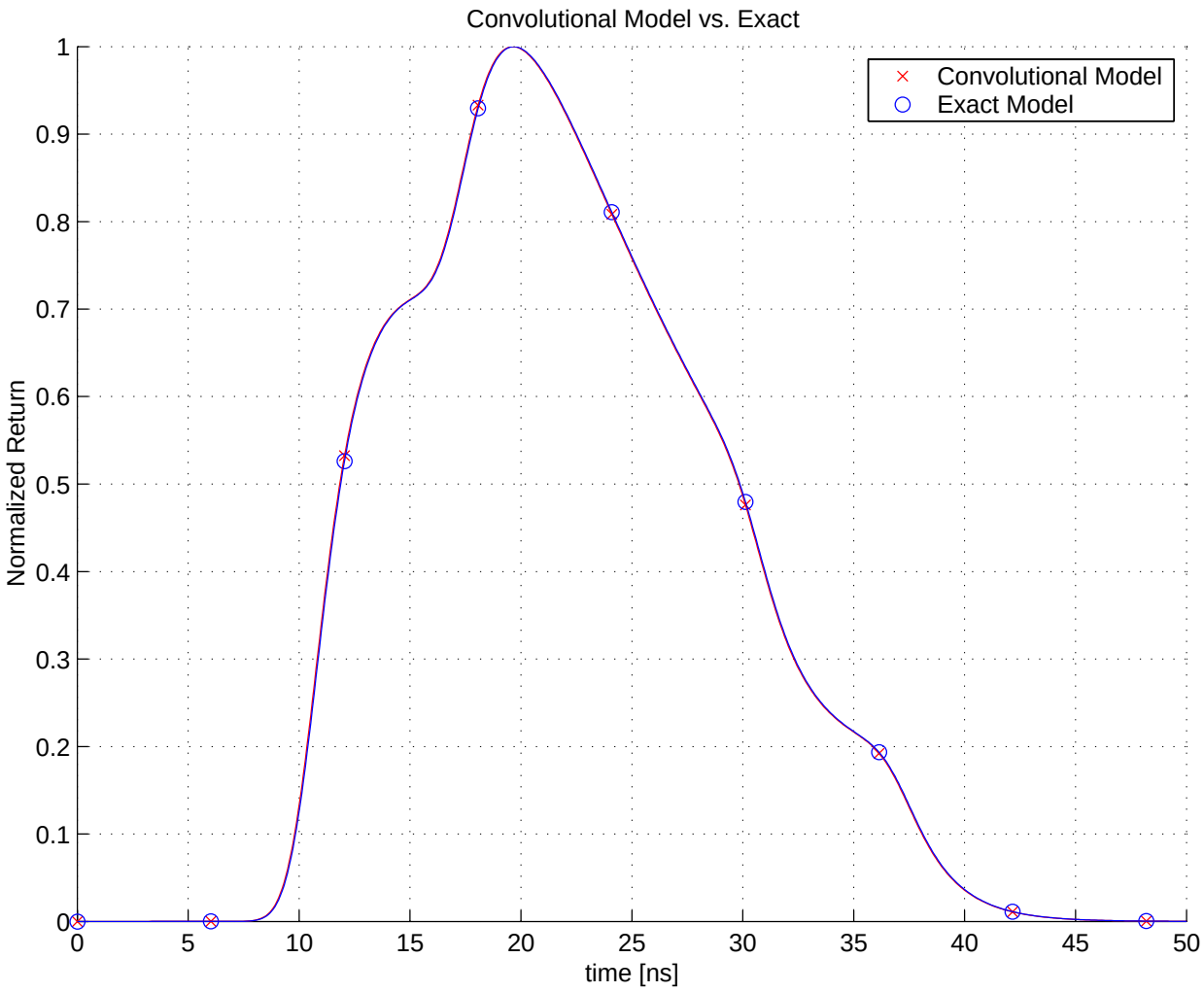

Figure 5.12: Comparison of convolutional model and exact model for a beamwidth of 1.0°.

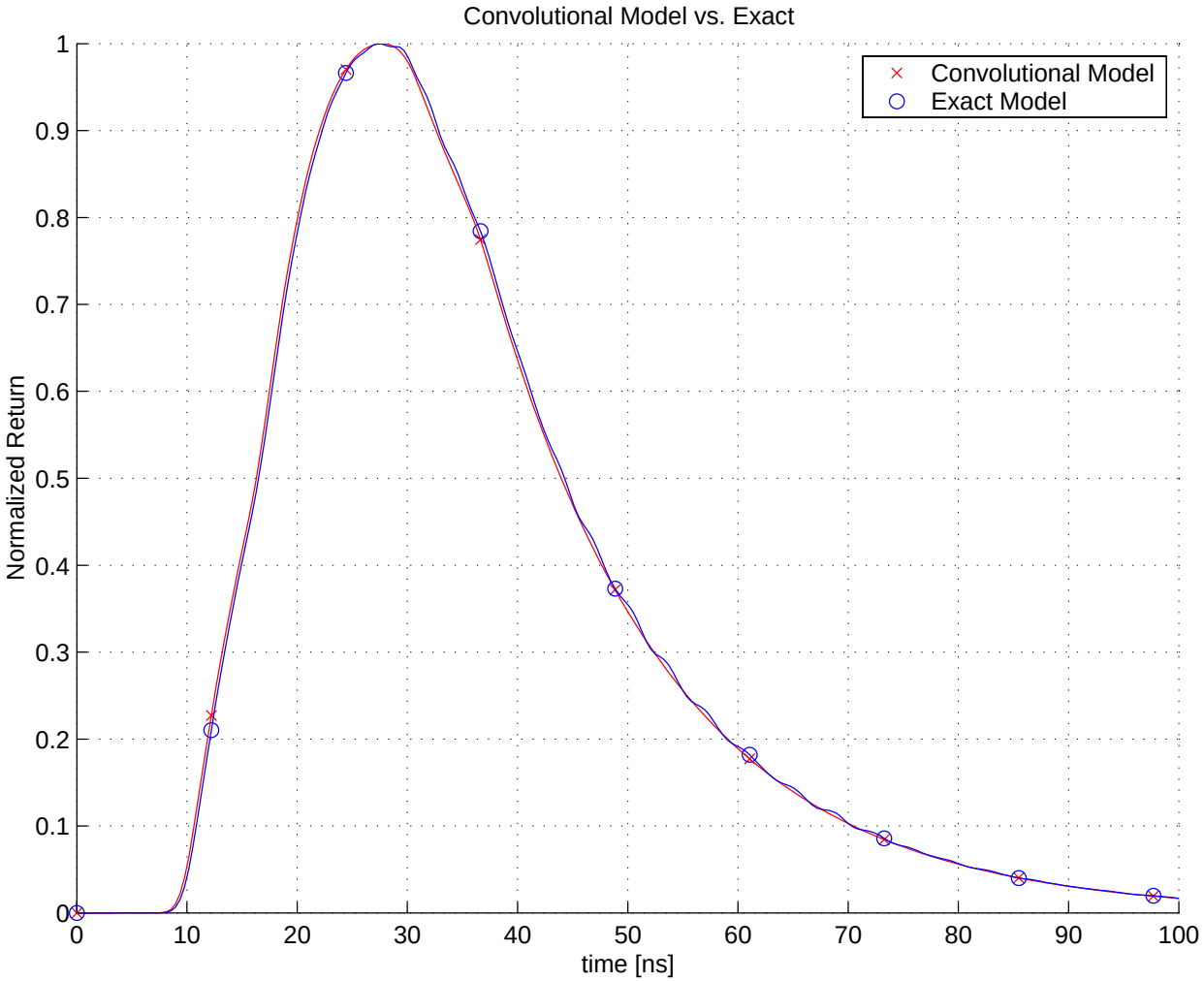

Figure 5.13: Comparison of convolutional model and exact model for a beamwidth of 3.0°.

5.8 Summary

In this chapter it was shown that the first-order polarimetric impulse response for a random volume of scatterers can be derived from the first-order solution to the radiative transfer equation. Through a change of variables, the volume scattering integration over the elevation variable, z, is easily shown to be a convolution of the incident waveform with a scattering and attenuation term obtained directly from radiative transfer and radar polarimetry theory. In its most basic form, the first order PVSIR can be expressed as

$$P_r = \frac{\lambda^2}{(4\pi)^3} \int_S P_t \left(t - 2\frac{r_i'}{c_o'} \right) \otimes \frac{G^2(\theta', \phi')}{(r_i')^4} \left[\sum_{n=1}^{N} 4\pi \cos\theta' \mathcal{P}_n'(t) \right] dS'.$$

If it can be assumed that the antenna is sufficiently narrow-beam and the platform height is much larger than the foliage depth, then this expression can further be simplified to

$$P_r(t) = P_t(t) \otimes P_{FS}(t) \otimes P_{VI}(t).$$

However, care must be taken when using these assumptions to assure that the phase matrix and resulting polarization signature are indeed independent of the angle, θ' over the antenna beamwidth. The developed model accounts for attenuation and single backscatter interaction by using the radar equation to account for propagation down to and back from the random volume interface, and radiative transfer theory to account for the propagation in the scattering medium.

Chapter 6

Conclusions and Future Work

This thesis has primarily dealt with the development of a new model for the incoherent power waveform scattered by layered vegetation. Starting with the time-harmonic Vector Radiative Transfer Equation, a ray-tracing approach was developed and used to incorporate time-dependence into existing first-order solutions to the VRTE. These expressions were identical to those obtained from other authors who used a rigorous Fourier analysis approach. Using Radiative Transfer theory in conjunction with the radar equation, the Polarimetric Volume Surface Impulse Response (PVSIR) was derived which computed the average backscattered waveform resulting from an arbitrarily polarized wave incident on a random volume. It was also shown that the single scatter mechanism in the volume resulted in a convolution of the incident waveform with a term obtained directly from radiative transfer. The convolution expression, which can be used in both traditional radiative transfer theory as well as in the PVSIR developed in this report is advantageous in that it eliminates the need to perform numerical integrations at several time steps and instead can be quickly and accurately computed using Fast Fourier Transforms. The model created herein was limited by the underlying RT theory used to construct it, and is therefore limited to situations in which the ratio of scattering to absorption is small, as well as to situations in which the fractional volume of the scatterers is less than 1%. Despite these restrictions, the model can be applied to most foliage canopy situations where both of these criterion are met.

At the time that this was written, physical measurements were unavailable for comparison. Future efforts involving this model should first be validated against appropriate measurements. One such system which recently was implemented by NASA is the Scanning Lidar Imager of Canopies by Echo Recovery (SLICER). Models have been created which account for both single [Sun and K.J.Ranson, 2000] and multiple [Kotchenova et al., 2003] scattering in the lidar returns. These models are based on a similar form of the radiative transfer equation and compare favorably with the SLICER returns, however, the transfer theories

developed are not based on electromagnetic interactions of scatterer particles and are therefore difficult to compare with the PVSIR. Furthermore, the models and SLICER system is restricted to the scalar problem, thereby the polarized VSIR model cannot be fully tested against the scalar returns of the SLICER data. Furthermore, [Kotchenova et al., 2003] have speculated that higher-order interactions within the foliage, which are not accounted for in the PVSIR, may be present in Lidar returns of certain forest types. Nevertheless, comparison with the SLICER data may prove useful in future implementations.

While the primary topic of this report was the application of the PVSIR and convolutional models to the realm of remote sensing of forests, it should also be noted that radiative transfer applies equally well to many other instances such as rain and fog [Ishimaru and Cheung, 1980] and ice sheets [Adams and Brown, 1998]. As more field measurements may be available for these scattering scenarious, the PVSIR developed in this paper should be expanded upon to model non-vegetative scattering. Consequently, background dielectrics and non-diffuse boundaries should be added to this method in order to account for alternative random volume scattering scenarios and remote sensing of different regions. Fortunately, the iterative solution to the VRTE can again be used to "add-in" these effects with minimal complexity.

Bibliography

[Adams and Brown, 1998] Adams, R. J. and Brown, G. S. (1998). A model for altimeter returns from penetrable geophysical media. *IEEE Trans. Geosci. Remote Sensing*, 36(5):1784–1793.

[Arfken, 1985] Arfken, G. (1985). *Mathematical Methods for Physicists*, pages 198–201. Academic Press, New York, third edition.

[Brown, 1977] Brown, G. S. (1977). The average impulse response of a rough surface and its applications. *IEEE Trans. Antennas Propagat.*, 25(1):67–74.

[Brown, 1990] Brown, G. S. (1990). Quasi-specular scattering from the air-sea interface. In Geernaert, G. and Plant, W., editors, *Surface Waves and Fluxes*, volume 2, pages 1–13. Kluwer Academic Publishers, Amsterdam, The Netherlands.

[Chandrasekhar, 1960] Chandrasekhar, S. (1960). *Radiative Transfer*. Dover Publications, Dover, NY.

[Chang and Jin, 2002] Chang, M. and Jin, Y. (2002). The temporal mueller matrix solution for polarimetric scattering from a layer of random non-spherical scatterers. *J. of Quant. Spect. & Rad. Trans.*, 74:339–353.

[Chang and Jin, 2003] Chang, M. and Jin, Y. (2003). The temporal mueller matrix solution for polarimetric scattering from inhomogeneous random media of non-spherical scatterers. *IEEE Trans. Antennas Propagat.*, 51(4):820–832.

[Collin, 1985] Collin, R. (1985). *Antennas and Radiowave Propagation*. McGraw Fill, New York, NY.

[Davis, 2000] Davis, B. (2000). *Propagation and Scattering of Waves by Terrain Features*. PhD thesis, Virginia Polytechnic Institute and State University, Blacksburg.

[Ishimaru, 1991] Ishimaru, A. (1991). *Electromagnetic Wave Propagation, Radiation and Scattering*. Prentice Hall, Englewood Cliffs, NJ.

[Ishimaru, 1997] Ishimaru, A. (1997). *Wave Propagation and Scattering in Random Media*. IEEE Press, New York, NY.

[Ishimaru and Cheung, 1980] Ishimaru, A. and Cheung, R.-T. (1980). Multiple scattering effects on wave propagation due to rain. *Ann. Telecommun*, 35:373–379.

[Ishimaru et al., 2001] Ishimaru, A., Jaruwatanadilok, S., and Kuga, Y. (2001). Polarized pulse waves in random discrete scatterers. *J. Opt. Soc. Amer.*, 40(1):5495–5502.

[Ishimaru and Yeh, 1984] Ishimaru, A. and Yeh, C. (1984). Matrix representations of the vector radiative transfer theory for randomly distributed nonspherical particles. *J. Opt. Soc. Amer.*, 1(4):359–364.

[Karam et al., 1988] Karam, M. et al. (1988). Electromagnetic wave scattering from some vegetation samples. *IEEE Trans. Geosci. Remote Sensing*, 26(6):799–808.

[Karam et al., 1992] Karam, M. et al. (1992). A microwave scattering model for layered vegetation. *IEEE Trans. Geosci. Remote Sensing*, 30(4):767–784.

[Karam and Fung, 1983] Karam, M. and Fung, A. (1983). Scattering from randomly oriented circular discs with application to vegetation. *Radio Science*, 18(4):557–565.

[Karam and Fung, 1989] Karam, M. and Fung, A. (1989). Leaf-shape effects in electromagnetic wave scattering. *IEEE Trans. Geosci. Remote Sensing*, 27(6):687–697.

[Kotchenova et al., 2003] Kotchenova, S. et al. (2003). Modeling lidar waveforms with time-dependent stochastic radiative transfer theory for remote estimations of forest structure. *Journal of Geophysical Research*, 108(D15):12.1 – 12.13.

[Lam and Ishimaru, 1994] Lam, C. M. and Ishimaru, A. (1994). Mueller matrix calculation for a slab of random medium with both random rough surfaces and discrete particles. *IEEE Trans. Antennas Propagat.*, 42(2):145–155.

[Liang et al., 2005a] Liang, P., Moghaddam, M., and Pierce, L. E. (2005a). Radiative transfer model for microwave bistatic scattering from forest canopies. *IEEE Trans. Geosci. Remote Sensing*, 43(5):2470–2483.

[Liang et al., 2005b] Liang, P., Moghaddam, M., Pierce, L. E., and Lucas, R. M. (2005b). Radar backscattering model for multilayer mixed-species forests. *IEEE Trans. Geosci. Remote Sensing*, 43(5):2612–2626.

[Newkirk and Brown, 1992] Newkirk, M. and Brown, G. (1992). Issues related to waveform computations for radar altimeter applications. *IEEE Trans. Antennas Propagat.*, 40(12):1478–1488.

[Newkirk and Brown, 1994] Newkirk, M. and Brown, G. (1994). An altimeter waveform model for combined surface and volume scattering. Technial Report EMIL-94-1, Electromagnetic Interactions Laboratory, Virginia Tech, Blacksburg, VA.

[Newkirk and Brown, 1996] Newkirk, M. and Brown, G. (1996). A waveform model for surface and volume scattering from ice and snow. *IEEE Trans. Antennas Propagat.*, 34(2):444–456.

[Rahmat-Samii, 1979] Rahmat-Samii, Y. (1979). Useful coordinate transforms for antenna applications. *IEEE Trans. Antennas Propagat.*, 27(4):571–574.

[Sandia National Laboratories, 2005] Sandia National Laboratories (2005). Ku-band synthetic aperture radar: Washington, DC from www.sandia.gov/radar/images/dc_big.jpg.

[Sun and K.J.Ranson, 2000] Sun, G. and K.J.Ranson (2000). Modeling lidar returns from forest canopies. *IEEE Trans. Geosci. Remote Sensing*, 38(6):2617 – 2626.

[Tsang and Ding, 1991] Tsang, L. and Ding, K.-H. (1991). Polarimetric signatures of a layer of random nonspherical discrte scatterers overlying a homogeneous half-space based on first- and second- order vector radiative transfer theory. *IEEE Trans. Antennas Propagat.*, 29(2):242–253.

[Tsang et al., 1985] Tsang, L., Kong, J., and Shin, R. (1985). *Theory of Remote Sensing*. Wiley, New York, NY.

[Ulaby and El Rayes, 1987] Ulaby, F. and El Rayes, M. (1987). Microwave dielectric spectrum of vegetation, part ii: Dual dispersion model. *IEEE Trans. Geosci. Remote Sensing*, 25:550–557.

[Ulaby and Elachi, 1990] Ulaby, F. and Elachi, C. (1990). *Radar Polarimetry for Geoscience Applications*. Artech House, Norwood, MA.

[Ulaby et al., 1990] Ulaby, F. et al. (1990). Michigan microwave canopy scattering model. *Int. J. Remote Sensing*, 11(7):1223–1253.

[Ulaby et al., 1986] Ulaby, F., Moore, R., and Fung, A., editors (1986). *From Theory to Applications*, volume 3 of *Microwave Remote Sensing: Active and Passive*. Artech House, Norwood.

[Whitman et al., 1996] Whitman, G. M. et al. (1996). A transport theory of pulse propagation in a strongly forward scattering random medium. *IEEE Trans. Antennas Propagat.*, 44(1):118–128.

Appendix A

Nomenclature

Symbol	Name	Definition
I	Intensity	Scalar quantity used to represent incoherent power in the Radiative Transfer Equation.
$\mathbf{I}$	Stokes Parameters	4x1 vector of intensities used to represent a polarized intensity.
P	Phase Function	Function which represents the intensity scattered by a random volume into a given solid angle.
J	Source Function	Self emitted power from a random volume. AKA Thermal source.
$\mathbf{P}$	Phase Matrix	4x4 matrix representation of phase function for the VRTE.
$\mathbf{F}$	Scattering Matrix	2x2 Matrix to relate incident and scattered electric field for vertical and horizontal polarizations. AKA Scattering Tensor.
$\mathbf{L}$	Stokes Matrix	4x4 Matrix to relate incident and scattered intensities described by the Stokes parameters. AKA Mueller matrix.
κ_e	Extinction Matrix	4x4 matrix which represents the attenuation due to scattering and absorption by a random media on the incident Stokes parameters.
$\mathbf{T}, T$	Transformation Matrix	4x4 matrix resulting from the iterative solution to the VRTE for a multilayered random volume.
σ^o	Backscatter Coefficient	Represents the backscatter cross section of a surface per unit area, generally for linear polarizations.
$\mathcal{P}$	Polarization Signature	Remote sensing quantity similar to the backscatter coefficient for an arbitrary polarization. AKA Polarization response.
Λ	-	Used to denote an integrand of the transformation matrix.
A	-	Used to denote an integral in the transformation matrix.

Appendix B

Scattering Expressions

This section will present the expressions used to model the vegetation. All expressions can be found in various literature, and are presented here without derivation or explanation purely for reference.

B.1 Scattering from a Small Sphere

The phase matrix for a region small dielectric sphere of radius a and permittivity ϵ_s is given in [Tsang et al., 1985] as

$$\mathbf{P} = \begin{bmatrix} P_{11} & P_{12} & P_{13} & 0 \\ P_{21} & P_{22} & P_{23} & 0 \\ P_{31} & P_{32} & P_{33} & 0 \\ 0 & 0 & 0 & P_{44} \end{bmatrix}$$

where

$$\begin{aligned}
P_{11} &= w\left[\cos\theta_s\cos\theta_i\cos(\phi_s-\phi_i)+\sin\theta_s\sin\theta_i\right]^2 \\
P_{12} &= w\cos^2\theta_s\sin^2(\phi_s-\phi_i) \\
P_{13} &= w\left[\cos\theta_s\sin\theta_s\sin\theta_i\sin(\phi_s-\phi_i)+\cos^2\theta_s\cos\theta_i\sin(\phi_s-\phi_i)\cos(\phi_s-\phi_i)\right] \\
P_{21} &= w\cos^2\theta_i\sin^2(\phi_s-\phi_i) \\
P_{22} &= w\cos^2(\phi_s-\phi_i) \\
P_{23} &= -w\cos\theta_i\sin(\phi_s-\phi_i)\cos(\phi_s-\phi_i) \\
P_{31} &= -2w\left[\sin\theta_s\sin\theta_i\cos\theta_i\sin(\phi_s-\phi_i)-\cos\theta_s\cos^2\theta_i\cos(\phi_s-\phi_i)\sin(\phi_s-\phi_i)\right]
\end{aligned}$$

$$
\begin{aligned}
P_{32} &= 2w\cos\theta_s \sin(\phi_s-\phi_i)\cos(\phi_s-\phi_i) \\
P_{33} &= w\left[\sin\theta_s\sin\theta_i\cos(\phi_s-\phi_i)+\cos\theta_s\cos\theta_i\left(\cos^2(\phi_s-\phi_i)-\sin^2(\phi_s-\phi_i)\right)\right] \\
P_{44} &= -w\left[\sin\theta_s\sin\theta_i\cos(\phi_s-\phi_i)+\cos\theta_s\cos\theta_i\right] \\
w &= \frac{3}{8\pi}\kappa_s
\end{aligned}
$$

and the scattering coefficient is given by

$$\kappa_s = 2f_v k^4 a^3 \left|\frac{\epsilon_s-\epsilon}{\epsilon_s+2\epsilon}\right|.$$

where f_v is the fractional volume. The extinction matrix is a diagonal matrix with all elements equal to $\kappa_a+\kappa_s$ where the absorption coefficient is

$$\kappa_a = f_v * k\frac{\epsilon_s''}{\epsilon}\left|\frac{3\epsilon}{\epsilon_s+2\epsilon}\right|^2.$$

B.2 Scattering Tensor for GRG Disc & Needle

The scattering tensor for a circular disc using the generalized Rayleigh Gans (GRG) approach is found in [Karam and Fung, 1983] [Karam and Fung, 1989] and are given as

$$
\begin{aligned}
F_v v(\hat{s},\hat{i}) &= \frac{k^2(\epsilon_r-1)}{4\pi}v_o\left[a_N\sin\theta_i\sin\theta_s - a_T\cos\theta_i\cos\theta_s\cos(\phi_s-\phi_i)\right]\mu(\hat{s},\hat{i}) \\
F_h v(\hat{s},\hat{i}) &= \frac{k^2(\epsilon_r-1)}{4\pi}v_o\cos\theta_i\sin(\phi_s-\phi_i)a_T\mu(\hat{s},\hat{i}) \\
F_v h(\hat{s},\hat{i}) &= \frac{k^2(\epsilon_r-1)}{4\pi}v_o\cos\theta_s\sin(\phi_s-\phi_i)a_T\mu(\hat{s},\hat{i}) \\
F_h h(\hat{s},\hat{i}) &= \frac{k^2(\epsilon_r-1)}{4\pi}v_o\cos(\phi_s-\phi_i)a_T\mu(\hat{s},\hat{i})
\end{aligned}
$$

and

$$
\begin{aligned}
a_T &= \frac{1}{(\epsilon_r-1)g_T+1} \\
a_N &= \frac{1}{(\epsilon_r-1)g_N+1}.
\end{aligned}
$$

The corresponding values for discs and needles are given in Table B.1. Both the cylinder and needle can be rotated through the Euler's Transformation outlined in Chapter 2 to account

	Disc	Needle
Valid	$2k_o t\sqrt{\epsilon_r} << \lambda$	$2k_o a\sqrt{\epsilon_r} << \lambda$
	$t << a$	$t >> a$
v_o	$2\pi a^2 t$	$2\pi a^2 t$
g_T	$\frac{1}{2(m^2-1)}\left[\frac{m^2}{\sqrt{m^2-1}} sin^{-1}\left(\frac{\sqrt{m^2-1}}{m}\right) - 1\right]$	$\frac{m(m^2-1)}{2}\left[\frac{m}{m^2-1} + \frac{1}{2}\log\frac{m-1}{m+1}\right]$
g_N	$\frac{m^2}{m^2-1}\left[1 - \frac{1}{\sqrt{m^2-1}}\sin^{-1}\left(\frac{\sqrt{m^2-1}}{m}\right)\right]$	$(1-m^2)\left[\frac{1}{2}\log\left(\frac{m-1}{m+1}\right) + 1\right]$
m	$\frac{a}{h}$	$\sqrt{1-\left(\frac{a}{h}\right)^2}$
μ	$2\frac{J_1(Qa)}{Qa}$	$\frac{\sin Q}{Q}$
Q	$k_o\sqrt{\sin^2\theta_s + \sin^2\theta_i - 2\sin\theta_s\sin\theta_i\cos(\phi_s - \phi_i)}$	$kh\left(\cos\theta_i + \cos\theta_s\right)$

Table B.1: Equations for GRG Scatterers.

for an arbitrary off-axis rotation.

Vita

Tyler Christian Kramer was born in Reading, PA in 1982. In December 2004 he was awarded a Bachelor of Science in Electrical Engineering from Virginia Tech where he graduated magna cum laude and a Commonwealth Scholar. From 2004-2005 he was employed by NanoSonic Inc., Blacksburg, VA, as a research scientist. From 2005-2007 he was a Graduate Research Assistant in the ElectroMagnetic Interactions Laboratory (EMIL), directed by Dr. Gary Brown.